

TOPICAL REVIEW

Atomistic modeling of fracture

To cite this article: P Andric and W A Curtin 2019 *Modelling Simul. Mater. Sci. Eng.* **27** 013001

View the [article online](#) for updates and enhancements.

Recent citations

- [Intrinsic fracture behavior of Mg–Y alloys](#)
Eleanor Mak and W A Curtin
- [Role of stress triaxiality on ductile versus brittle fracture in pre-cracked FCC single crystals: an atomistic study](#)
Rajwinder Singh and Dhiraj K Mahajan
- [Atomistic approaches to cleavage of interfaces](#)
Miroslav erný *et al*



IOP | ebooks™

Bringing together innovative digital publishing with leading authors from the global scientific community.

Start exploring the collection—download the first chapter of every title for free.

Topical Review

Atomistic modeling of fracture

P Andric  and **W A Curtin**

Laboratory for Multiscale Mechanics Modeling, EPFL, CH-1015 Lausanne, Switzerland

E-mail: predrag.andric@epfl.ch

Received 17 July 2018, revised 12 September 2018

Accepted for publication 25 September 2018

Published 16 November 2018



CrossMark

Abstract

Atomistic modeling of fracture is intended to illuminate the complex response of atoms in the very high stressed region just ahead of a sharp crack. Accurate modeling of the atomic scale fracture is crucial for describing the intrinsic nature of a material (intrinsic ductility/brittleness), chemical effects in the crack-tip vicinity, the crack interaction with different defects in solids such as grain boundaries, solutes, precipitates, dislocations, voids, etc. Here, different methods for atomistic modeling of fracture are compared in their ability to obtain quantitatively useful results that are in agreement with the basic principles of linear elastic fracture mechanics (LEFM). We demonstrate that the complicated atomic crack-tip behavior is precisely described in simulations of semi-infinite cracks, where the loading is uniquely controlled by the applied stress intensity factor K . Such ‘ K -test’ simulations are shown to be equally applicable in crystalline and amorphous materials, and to be suitable for quantitative evaluation of various critical stress intensity factors, the overall material fracture toughness, and quantitative comparison with theories. We further demonstrate that the simulation of a nanoscale center-crack tension (CCT) specimen often leads to the results that do not satisfy the conditions for application of LEFM. The simulated intrinsic fracture toughness, one of the basic material properties, using CCT test geometry is shown to be dependent on the crack size and far-field loading. In general, this study resolves quantitative differences between several methods for atomistic modeling of fracture and recommends that application of simulations based on nanoscale finite size cracks not be pursued.

Keywords: linear elastic fracture mechanics, cracks, molecular statics simulations, dislocations, amorphous materials

(Some figures may appear in colour only in the online journal)

1. Introduction

Fracture mechanics is an indispensable tool in the design process of various structures (cars, airplanes, concrete dams, ...) that require high performance and high reliability. A constant demand for lower cost, lower weight, and improved energy efficiency drives the development of new materials, with the application of fracture mechanics in assessing material fracture toughness, fatigue, and embrittlement (e.g. stress corrosion cracking). The overall resistance of a material to crack growth is governed by processes across different length scales. For instance, large-scale dislocation plasticity provides the dominant toughening in metallic components while large-scale fiber-bridging provides the dominant toughening in fiber-reinforced composites. However, the fracture process itself is ultimately the separation of material, and is thus fundamentally atomistic in nature, indicating that an understanding of nanoscale fracture has value even for engineering-scale problems.

A number of important phenomena in fracture are indeed connected with atomistic/nanoscale behavior around a crack. The intrinsic nature of a material—is it brittle or ductile?—is dictated by whether an initial sharp crack will cleave (intrinsically brittle) or blunt by dislocation emission (intrinsically ductile) [1–3]. The attack of embrittling species at the crack tip, as in hydrogen embrittlement [4], involves detailed chemical interactions at the atomic scale. The behavior of cracks along, parallel to, or approaching grain boundaries, and the influence of chemical segregation to grain boundaries on fracture toughness are similarly intrinsically atomic scale issues. The interactions of cracks with nanoscale microstructure and defects (solute, precipitates, dislocations, voids, ...) also plays a role in establishing macroscopic fracture behavior.

Given the range of important nanoscale fracture phenomena that might be of interest in different situations, it is then natural to analyze problems using atomistic simulations so as to gain mechanistic, qualitative, and/or quantitative understanding. Such simulations encompass molecular statics or dynamics using either semi-empirical classical interatomic potentials or first-principles methods. The latter require advanced multiscale techniques and so will only be addressed at the end of this article. Pioneering work on atomistic modeling of fracture started almost five decades ago with studies on the influence of crystallographic orientation on crack propagation [5], and the effects of lattice trapping of cracks [6]. Due to the limited computational power, these early simulations were limited to a very small number of atoms, although work of Thomson *et al* [6] using Greens function methods presaged modern multiscale modeling. Increasing computer power has led to a concomitant increase in atomistic studies of fracture covering many of the topics mentioned above. We point to a few representative references for intrinsic brittle/ductile behavior [7–11], grain boundary fracture [12–15], H and other chemical embrittlement [15–20], and crack/defect interactions [21–25]. In this wide range of literature, various simulation methods have been used to probe phenomena qualitatively or quantitatively.

Not all simulation methods are equally useful for obtaining an accurate understanding of the phenomena. The broad focus of this article addresses the advantages and disadvantages of different methodologies, in terms of their ability to extract quantitatively accurate results that are faithful to the principles of fracture mechanics. Unfortunately, many publications use methods that strongly influence the outcomes of the simulations, and thus leading to inaccurate, if not incorrect, conclusions about fracture phenomena. The main point is that certain simulation methods for nanoscale cracks are often not directly relevant to the real behavior of larger cracks. Specifically, as we will show, the simulation of a nanoscale center-crack tension (CCT) specimen often precludes satisfying the conditions for the application of linear elastic fracture mechanics (LEFM); other finite crack geometries have the same problem. We

(the so-called fracture process zone (FPZ), occurring over a scale $r_{\text{FPZ}} \ll r_K$). When SSY is satisfied, i.e. $r_{\text{FPZ}} \ll r_K \ll a$, the crack tip behavior depends only on the asymptotic crack tip fields and not on the macroscopic loading conditions. This confers a huge generality to studies focused on the crack tip region. When SSY conditions are satisfied, phenomena observed and quantified in the FPZ as a function of the magnitude of the asymptotic field are relevant to all macroscopic fracture problems independent of loading and geometry. One can now immediately comprehend that problems wherein the typical crack size a itself is on the nanoscale cannot easily satisfy the SSY condition, or only satisfy the SSY condition at the scale of the atomic spacing, where the material response is intrinsically discrete. This introductory discussion presages our analyses below: failure to satisfy SSY conditions in nanoscale simulation studies invalidates the generality of the observed/measured results, making them non-transferable to the true problems of interest. Thus, atomistic simulation methods must be designed to satisfy SSY, and the applicability of SSY must be continually assessed as complex nonlinear/non-convex crack tip phenomena evolve under increasing load.

The remainder of this article is organized as follows. Due to the critical importance of LEFM, section 2 reviews the LEFM formalism, with a focus on the asymptotic stress and displacement fields around a crack tip and the scale of the K -dominant domain r_K . In section 3, we theoretically analyze the semi-infinite crack under K control (K -test), and the finite-size center-crack tension specimen (CCT test), as two most commonly used methods in atomistic modeling of fracture, with the focus on creating the atomically sharp crack presented in section 3.1. In section 4, we analyze simulation results obtained using both test geometries. We progress through problems involving the initial crack tip behavior (cleavage or dislocation emission) where $r_{\text{FPZ}} \sim a_0$ (lattice spacing) to situations after dislocation emission, using fcc Ni as a test material, and amorphous Li-Si that has non-dislocation plastic flow behavior and a void nucleation and linking mode of failure. Finally, in section 5 we briefly discuss the use of the K -test method in advanced multiscale methods such as couple atomistic discrete dislocations (CADDs), quantum-mechanical couple atomistic discrete dislocations (QM-CADD), and coupled QM and molecular mechanical (MM) in which the crack-tip region is at least one level more accurately described than the surrounding material. We then discuss the challenges with modeling 3D crack problems, and other issues that limit the use of atomistic models.

2. Linear elastic fracture mechanics in plane strain

2.1. Crack stress fields

Understanding of LEFM is a crucial requirement for performing accurate atomistic crack simulations. LEFM is well-established in a wide range of literature [30–33] but we revisit the key results here since they form the theoretical basis for creating useful simulation models.

We consider a large plate of lateral dimensions $-L/2 < x_1 < L/2$, $-L/2 < x_2 < L/2$ made of a linear isotropic material and subject to plane strain loading so that results are independent of the out-of-plane x_3 dimension. The plate contains a finite crack of a size $2a$ in the center $-a < x_1 < a$, $x_2 = 0$ with $a \ll L$. The crack is defined by the imposition of traction free boundary conditions on both the upper and lower crack surfaces. Here, we analyze the plate subjected to a biaxial stress σ^{app} applied on the outer boundaries with $L \rightarrow \infty$ (see figure 1(a)).

This loading scenario corresponds to the so-called Mode I fracture mode, where the crack is opened by a perpendicular tensile load. Mode II (in-plane shear) and Mode III (anti-plane

strain) are the other two independent modes of loading, but the general conclusions from the theory for Mode I apply equally to Mode II and Mode III loading, and so these are not discussed here. Although the Mode I biaxial loading may appear to be a special case even for Mode I, it will be shown below that the asymptotic singular stresses in the crack-tip vicinity do not depend on the geometry or the far-field loading. The outer boundary conditions for the problem are then

$$\begin{aligned} \sigma_{12} = \sigma_{22} &= 0 \text{ at } |x| \leq a \text{ and } y = 0 \\ \sigma_{11} = \sigma_{22} &= \sigma^{\text{app}} \text{ at } x_i^2 \rightarrow \infty \end{aligned} \quad (1)$$

In linear elasticity, components of the small strain tensor are related to components of the displacement field u_i as $\epsilon_{ij} = (u_{i,j} + u_{j,i})/2$, where $(\cdot)_{,i}$ denotes partial differentiation with respect to x_i . The stress tensor is related to the strain tensor via Hooke's law $\sigma_{ij} = C_{ijkl} \epsilon_{kl}$ where C_{ijkl} is the material stiffness tensor. We will start with isotropic elasticity and later generalize to anisotropic elasticity, since nearly all single crystal materials are anisotropic to some degree. The two independent elastic constants in isotropic elasticity are then taken as the shear modulus μ and Poisson ratio ν . The solution to the equilibrium equation in linear elasticity and the given boundary conditions can, for instance, be obtained using the complex potential method following the Kolosov–Muskhelishvili formulation [34]. The stress and displacement fields are given in terms of complex potentials as

$$\begin{aligned} \sigma_{11} + \sigma_{22} &= 4 \operatorname{Re} \{ \psi(z)_{,1} \} \\ \sigma_{22} - \sigma_{11} + 2i\sigma_{12} &= 2 \{ \bar{z}\psi(z)_{,2} + \chi(z)_{,2} \} \\ 2\mu(u_1 + iu_2) &= (3 - 4\nu)\psi(z) - z\bar{\psi(z)}_{,1} - \bar{\chi(z)}_{,1}, \end{aligned} \quad (2)$$

where $z = x_1 + ix_2$, and $\psi(z)$ and $\chi(z)$ are analytical complex functions to be determined. Since the crack fields will be singular at the crack tips, the complex functions must have the appropriate singularities. The solution of the unknown complex function $\psi(z)$ for the crack problem was introduced by Westergaard [35] as

$$\begin{aligned} \psi &= \frac{1}{2} \sigma^{\text{app}} \sqrt{z^2 - a^2} + Az \\ \psi_{,1} &= \frac{\sigma^{\text{app}} z}{\sqrt{z^2 - a^2}} + A, \end{aligned} \quad (3)$$

where A is a real valued constant. Since the far-field loading is symmetric with respect to the x_1 axis, the shear stress $\sigma_{12} = 0$ along $x_2 = 0$. This leads to the unique relation between $\psi(z)$ and $\chi(z)$ as

$$\chi(z)_{,2} + \bar{z}\psi(z)_{,2} + A = 0. \quad (4)$$

For the present case of biaxial tension $A = 0$ while for uniaxial tension $A = \sigma^{\text{app}}/2$. The stress field associated with A does not contribute to the crack-tip singularity. Substituting equations (3) and (4) into (2) yields a solutions for the unknown stress field that is most conveniently expressed in terms of the polar coordinates (see figure 1(a)) with

$$\begin{aligned} z &= re^{i\theta} \\ z - a &= r_1 e^{i\theta_1} \\ z + a &= r_2 e^{i\theta_2}. \end{aligned} \quad (5)$$

With this notation, the stress field is

$$\begin{aligned}\sigma_{11} &= \frac{\sigma^{\text{app}}_r}{\sqrt{r_1 r_2}} \left[\cos \left(\theta - \frac{1}{2}\theta_1 - \frac{1}{2}\theta_2 \right) - \frac{a^2}{r_1 r_2} \sin \theta \sin \frac{3}{2}(\theta_1 + \theta_2) \right] \\ \sigma_{22} &= \frac{\sigma^{\text{app}}_r}{\sqrt{r_1 r_2}} \left[\cos \left(\theta - \frac{1}{2}\theta_1 - \frac{1}{2}\theta_2 \right) + \frac{a^2}{r_1 r_2} \sin \theta \sin \frac{3}{2}(\theta_1 + \theta_2) \right] \\ \sigma_{12} &= \frac{\sigma^{\text{app}}_r}{\sqrt{r_1 r_2}} \left[\frac{a^2}{r_1 r_2} \sin \theta \cos \frac{3}{2}(\theta_1 + \theta_2) \right].\end{aligned}\quad (6)$$

2.2. Asymptotic near-tip stress fields

The stress fields close to the crack tip are of fundamental importance in fracture mechanics. These asymptotic fields are obtained by taking the limits $\sigma_{ij} \rightarrow \infty$ as $r_i \rightarrow 0$, with various terms above reducing to

$$\begin{aligned}\frac{r_1}{a} &\ll 1, \quad \theta \approx 0, \quad \theta_2 \approx 0 \\ r &\approx a, \quad r_2 \approx 2a \\ \sin \theta &\approx \frac{r_1}{a} \sin \theta_1 \\ \sin \frac{3}{2}(\theta_1 + \theta_2) &\approx \sin \frac{3}{2}\theta_1 \\ \cos \left(\theta - \frac{1}{2}\theta_1 - \frac{1}{2}\theta_2 \right) &\approx \cos \frac{1}{2}\theta_1 \\ \cos \frac{3}{2}(\theta_1 + \theta_2) &\approx \cos \frac{3}{2}\theta_1\end{aligned}\quad (7)$$

and thus leading to the asymptotic near-tip stress state

$$\begin{aligned}\sigma_{11} &= \frac{\sigma^{\text{app}}_a}{\sqrt{2ar_1}} \cos \frac{1}{2}\theta_1 \left(1 - \sin \frac{1}{2}\theta_1 \sin \frac{3}{2}\theta_1 \right) \\ \sigma_{22} &= \frac{\sigma^{\text{app}}_a}{\sqrt{2ar_1}} \cos \frac{1}{2}\theta_1 \left(1 + \sin \frac{1}{2}\theta_1 \sin \frac{3}{2}\theta_1 \right) \\ \sigma_{12} &= \frac{\sigma^{\text{app}}_a}{\sqrt{2ar_1}} \sin \frac{1}{2}\theta_1 \cos \frac{1}{2}\theta_1 \cos \frac{3}{2}\theta_1.\end{aligned}\quad (8)$$

Shifting the coordinate system to be centered on the crack tip ($r, \theta_1 \equiv \theta$), the near-tip can be expressed in terms of the Mode I *stress intensity factor* K_I as

$$\begin{aligned}\sigma_{11} &= \frac{K_I}{\sqrt{2\pi r}} \cos \frac{1}{2}\theta \left(1 - \sin \frac{1}{2}\theta \sin \frac{3}{2}\theta \right) \\ \sigma_{22} &= \frac{K_I}{\sqrt{2\pi r}} \cos \frac{1}{2}\theta \left(1 + \sin \frac{1}{2}\theta \sin \frac{3}{2}\theta \right) \\ \sigma_{12} &= \frac{K_I}{\sqrt{2\pi r}} \sin \frac{1}{2}\theta \cos \frac{1}{2}\theta \cos \frac{3}{2}\theta\end{aligned}\quad (9)$$

with K_I for this problem defined as [36]

$$K_I = \sigma^{\text{app}} \sqrt{\pi a}. \quad (10)$$

The asymptotic stress field is thus independent of the particular applied stress or crack length, and only depends on the combination through the Mode I stress intensity factor.

Equation (9) reveals the well-known inverse square root singularity at the crack-tip, with the magnitude of the singularity controlled by the stress intensity factor K_I . Although equation (9) has been derived for a very specific loading case (see figure 1(a)), the asymptotic near-tip stress fields are *independent* of the geometry and boundary conditions. K_I uniquely characterizes the singular stress field near the crack tip, and does not depend on the material properties. The value of K_I is determined by the entire problem geometry and crack shape, but the crack tip behavior can be entirely characterized in terms of phenomena occurring as a function of the single loading parameter K_I . For complex geometries and loadings, the crack tip field depends on the three loading parameters K_I , K_{II} , and K_{III} ; we focus on K_I for simplicity and because it is usually more important than the other loading modes.

The asymptotic displacement fields around the crack tip can be derived in a similar manner, leading to

$$\begin{aligned} u_1 &= \frac{K_I}{\mu} \sqrt{\frac{r}{2\pi}} \cos \frac{\theta}{2} \left(1 - 2\nu + \sin^2 \frac{\theta}{2} \right) \\ u_2 &= \frac{K_I}{\mu} \sqrt{\frac{r}{2\pi}} \sin \frac{\theta}{2} \left(2 - 2\nu - \cos^2 \frac{\theta}{2} \right). \end{aligned} \quad (11)$$

Note that equation (11) is only valid for the plane-strain approximation.

The isotropic results of equations (9) and (11) can be generalized to full anisotropic elasticity [37]. Atomistic simulations often deal with crystalline materials that are elastically anisotropic. Macroscopic isotropy only emerges in aggregates of polycrystals. Thus, detailed simulation and interpretation of atomistic simulation results requires the application of anisotropic elasticity and/or a quantitative understanding of the differences created by using isotropic models to understand anisotropic materials. A very detailed and complete description of the general formalism developed by Stroh and its application to fracture problems can be found in chapters 5 and 11, respectively, of '*Anisotropic Elasticity: Theory and Application*' by Ting [37], and hence we only summarize the major results here. The anisotropic stress fields are

$$\begin{aligned} [\sigma_{11}, \sigma_{21}, \sigma_{31}]^T &= -\frac{K_I}{\sqrt{2\pi r}} \operatorname{Re} \left\{ \mathbf{B} \left\langle \frac{v_\alpha}{\sqrt{\cos \theta + v_\alpha \sin \theta}} \right\rangle \mathbf{B}^{-1} \right\} \\ [\sigma_{12}, \sigma_{22}, \sigma_{32}]^T &= -\frac{K_I}{\sqrt{2\pi r}} \operatorname{Re} \left\{ \mathbf{B} \left\langle \frac{1}{\sqrt{\cos \theta + v_\alpha \sin \theta}} \right\rangle \mathbf{B}^{-1} \right\} \end{aligned} \quad (12)$$

for the near tip stress state. The angle bracket notation in equation (12) and subsequently below is used to represent elements of an diagonal matrix. The corresponding near tip displacement fields are

$$\mathbf{u} = K_I \sqrt{\frac{2r}{\pi}} \operatorname{Re} \{ \mathbf{A} \langle \sqrt{\cos \theta + v_\alpha \sin \theta} \rangle \mathbf{B}^{-1} \}, \quad (13)$$

where v , \mathbf{A} and \mathbf{B} satisfy the following eigenvalue equation

$$\mathbf{N} \begin{bmatrix} \mathbf{A} \\ \mathbf{B} \end{bmatrix} = \mathbf{v} \begin{bmatrix} \mathbf{A} \\ \mathbf{B} \end{bmatrix}. \quad (14)$$

In equation (14) $\mathbf{v} = \langle v_\alpha \rangle = \text{diag}[v_\alpha]$ are the eigenvalues defined in the Stroh formalism, $\mathbf{A} = [\mathbf{a}_1, \mathbf{a}_2, \mathbf{a}_3]$ and $\mathbf{B} = [\mathbf{b}_1, \mathbf{b}_2, \mathbf{b}_3]$ are complex matrices composed of eigenvectors \mathbf{a} and \mathbf{b} , and \mathbf{N} is the *fundamental elasticity matrix* [38] defined as

$$\mathbf{N} = \begin{bmatrix} \mathbf{N}_1 & \mathbf{N}_2 \\ \mathbf{N}_3 & \mathbf{N}_1^T \end{bmatrix} \quad (15)$$

with

$$\mathbf{N}_1 = -\mathbf{T}^{-1}\mathbf{R}^T, \quad \mathbf{N}_2 = \mathbf{T}^{-1}, \quad \mathbf{N}_3 = \mathbf{R}\mathbf{T}^{-1}\mathbf{R}^T - \mathbf{Q} \quad (16)$$

and

$$\mathbf{Q} = \begin{bmatrix} C_{11} & C_{16} & C_{15} \\ C_{16} & C_{66} & C_{56} \\ C_{15} & C_{56} & C_{55} \end{bmatrix}, \mathbf{R} = \begin{bmatrix} C_{16} & C_{12} & C_{14} \\ C_{66} & C_{26} & C_{46} \\ C_{56} & C_{25} & C_{45} \end{bmatrix}, \mathbf{T} = \begin{bmatrix} C_{66} & C_{26} & C_{46} \\ C_{26} & C_{22} & C_{24} \\ C_{46} & C_{24} & C_{44} \end{bmatrix}. \quad (17)$$

C_{ij} in equation (17) are the components of the material stiffness tensor written in the contracted (Voigt) notation. A closed form analytical solution can be derived when the material properties are symmetric about the crack line [31], leading to

$$\begin{aligned} \sigma_{11} &= \frac{K_I}{\sqrt{2\pi r}} \text{Re} \left[\frac{a_1 a_2}{a_1 - a_2} \left(\frac{a_2}{\sqrt{\cos \theta + a_2 \sin \theta}} - \frac{a_1}{\sqrt{\cos \theta + a_1 \sin \theta}} \right) \right] \\ \sigma_{22} &= \frac{K_I}{\sqrt{2\pi r}} \text{Re} \left[\frac{1}{a_1 - a_2} \left(\frac{a_1}{\sqrt{\cos \theta + a_2 \sin \theta}} - \frac{a_2}{\sqrt{\cos \theta + a_1 \sin \theta}} \right) \right] \\ \sigma_{12} &= \frac{K_I}{\sqrt{2\pi r}} \text{Re} \left[\frac{a_1 a_2}{a_1 - a_2} \left(\frac{1}{\sqrt{\cos \theta + a_1 \sin \theta}} - \frac{1}{\sqrt{\cos \theta + a_2 \sin \theta}} \right) \right] \end{aligned} \quad (18)$$

for the near-tip stress state and

$$\begin{aligned} u_1 &= K_I \sqrt{\frac{2r}{\pi}} \text{Re} \left[\frac{1}{a_1 - a_2} (a_1 p_2 \sqrt{\cos \theta + a_2 \sin \theta} - a_2 p_1 \sqrt{\cos \theta + a_1 \sin \theta}) \right] \\ u_2 &= K_I \sqrt{\frac{2r}{\pi}} \text{Re} \left[\frac{1}{a_1 - a_2} (a_1 q_2 \sqrt{\cos \theta + a_2 \sin \theta} - a_2 q_1 \sqrt{\cos \theta + a_1 \sin \theta}) \right] \end{aligned} \quad (19)$$

for the near tip displacement fields, where p_1, p_2, q_1 and q_2 depend on the material elastic properties. These constants can be found from

$$\begin{aligned} p_1 &= S_{11}^p a_1^2 + S_{12}^p - S_{16}^p a_1 \\ p_2 &= S_{11}^p a_2^2 + S_{12}^p - S_{16}^p a_2 \\ q_1 &= S_{12}^p a_1 + S_{22}^p / a_1 - S_{26}^p \\ q_2 &= S_{12}^p a_2 + S_{22}^p / a_2 - S_{26}^p, \end{aligned} \quad (20)$$

where a_1 and a_2 are roots of the following characteristic equation

$$S_{11}^p a^4 - 2S_{16}^p a^3 + (2S_{12}^p + S_{66}^p) a^2 - 2S_{26}^p a + S_{22}^p = 0 \quad (21)$$

and $S_{ij}^p = S_{ij} - S_{i3}S_{3j}/S_{33}$, where $\mathbf{S} = \mathbf{C}^{-1}$, are components of the material compliance tensor for the plane strain approximation, when expressed in the Voigt notation. The above equations are slightly unwieldy, but easily computed. Thus, there is little impediment to the application of full anisotropic elasticity in simulations and their interpretation when using the K -test methodology (see below). For the CCT specimen, which involves only traction boundary conditions, the simulation method is independent of the anisotropy. However, the crack tip fields follow the anisotropic results since the material is anisotropic; interpretation thus still requires knowledge of the anisotropic fields.

2.3. K -dominance zone

The asymptotic crack tip fields are controlled by the stress intensity factor K_I . However, the domain over which the asymptotic fields dominate the non-asymptotic fields depends on the crack size. In atomistic simulations, which are always at a small scale, we generally aim to extract intrinsic crack tip behavior, i.e. behavior that is not dependent on sample size, shape, crack size, or far-field loading. That is, we seek the intrinsic behavior that is controlled by K_I . It is therefore essential that all inelastic crack tip phenomena occur within the region where the asymptotic fields are dominant. Since we have the entire stress field for the center-crack problem (equation (6)) and the asymptotic fields (equation (9)), we can examine the relative contributions of the asymptotic and non-asymptotic fields.

The *degree of K -dominance* is usually assessed using the opening stress σ_{22} along the x_1 line ahead of the crack. The degree of K -dominance Λ is then defined as [31]

$$\Lambda = \frac{\sigma_{22}^{\text{singular}}}{\sigma_{22}^{\text{singular}} + \sigma_{22}^{\text{nonsingular}}}, \quad (22)$$

where $\sigma_{22}^{\text{singular}} = K_I/\sqrt{2\pi x_1}$, ($x_1 > 0$, $\theta = 0$), is the singular opening stress ahead of the crack tip and

$$\sigma_{22}^{\text{singular}} + \sigma_{22}^{\text{nonsingular}} = \frac{(x_1 + a)\sigma^{\text{app}}}{\sqrt{x_1(x_1 + 2a)}}, \quad (x_1 > 0, \theta = 0) \quad (23)$$

is the total stress ahead of the crack-tip derived from equation (6), and rewritten for the coordinate system positioned at the right tip. Recalling that $K_I = \sigma^{\text{app}}\sqrt{\pi a}$, equation (22) can be rewritten as

$$\Lambda = \frac{\sqrt{1 + x_1/2a}}{(1 + x_1/a)} \approx 1 - 3x_1/4a. \quad (24)$$

A typical estimate of the radius r_K within which the asymptotic field dominates is obtained by setting $\Lambda \geq 0.90$, leading to $r_K = x_K \approx 0.15a$ for $\Lambda = 0.90$. Other choices for Λ yield different estimates but the major outcome is that the domain of K -dominance is always much smaller than the half-crack size a . As an explicit example, figure 2 shows the stress field $\sigma_{22}(x_1, x_2 = 0)$ obtained from an atomistic simulation of a center-crack specimen in Ni, for various crack sizes a and loads having the same K_I ; details of such simulation are explained in section 4.1. When presented in double-log form, the asymptotic square root singularity appears nicely and the deviations from the asymptotic field with increasing distance from the crack tip (whose location is itself not exact) are easily identified. For a crack of size $a_{\text{min}} \approx 18 \text{ \AA}$, notable deviations appear at distances $\approx 3 \text{ \AA}$. For the largest crack, $a = 140 \text{ \AA}$, requiring a simulation domain of $L \approx 300 \text{ nm}$ containing ~ 7.7 million atoms at $T = 0 \text{ K}$, deviations from the asymptotic field are evident at a distance of $\approx 40 \text{ \AA}$. The simulation results

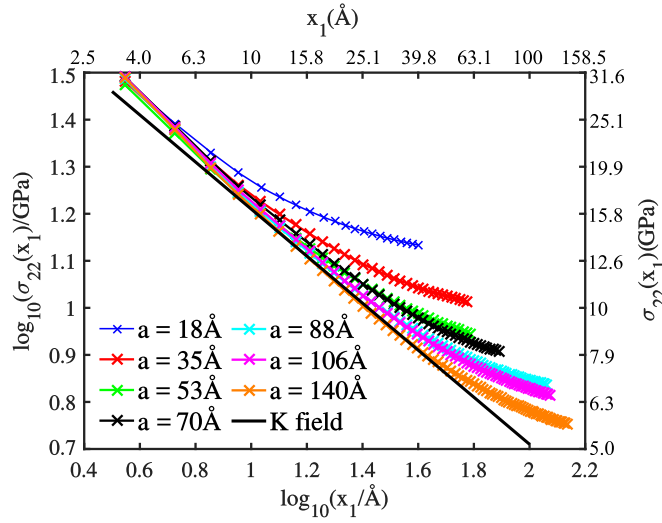


Figure 2. Atomic opening stress $\sigma_{22}(x_1 > 0, x_2 = 0)$ versus distance from the crack tip, for crack sizes considered here as observed in simulations within the ‘brittle’ crystal orientation. The asymptotic singular stress given by equation (18) is also shown (black line). The use of a log–log reveals the K -field singularity of $\frac{1}{2}$.

are thus fully consistent with the analytic estimate for $r_K = \frac{4}{3}(1 - \Lambda)a$, and hence this estimate can be used to design relevant simulation sizes.

2.4. Crack-tip processes: the fracture process zone

The diverging stresses at the crack tip that are predicted by LEFM are, of course, resolved to finite values due to nonlinear response of the real material at very high stresses. Figure 2 at value $K_I \approx 0.92 \text{ MPa } \sqrt{\text{m}}$ shows crack tip stresses on the order of $\sim 30 \text{ GPa}$, for instance. The local failure of LEFM does not, however, negate the role of K_I as the relevant loading parameter. The deviations from linear behavior can be thought of as perturbations that are self-equilibrating locally. The deviations do not generate additional long-range fields but are only dipolar ($1/r^2$ in 2d). Therefore, all of the energetic changes in the system are also localized around the region of nonlinear behavior, and this domain is termed the ‘fracture process zone (FPZ)’ with characteristic scale r_{FPZ} around the tip. As long as the nonlinear behavior is well-confined within the K -dominant domain, $r_{\text{FPZ}} \ll r_K$, the asymptotic fields at $r \approx r_K$ are unchanged, and the fields beyond r_K are also unchanged. The present qualitative discussion is formally proven by Rice [28] and Willis [29].

The major quantity of interest in atomistic modeling of fracture is the effective fracture toughness, i.e. the resistance of the material to crack growth including all of the near-tip energy-dissipating processes that may occur in the FPZ. Since loading is determined entirely by K_I , the fracture toughness is equal to the critical stress intensity K_{Ic} at which the crack extends. The critical stress intensity K_{Ic} may evolve as the crack grows, due to an evolving size of the FPZ and associated increase in energy dissipation by FPZ processes. This is captured through the notion of a crack-resistance curve, or R -curve, $K_{\text{Ic}} = K_{\text{Ic}}(\Delta a)$ where Δa is the extent of crack growth. During crack growth, it remains necessary that the entire evolving FPZ stays within the K -dominant regime.

2.5. Crack-tip processes: stress intensity and energetic perspectives

Since the fracture toughness is determined by energy-dissipating processes in the FPZ, it is also convenient to formulate the fracture problem in an energetic framework. To this end, one can define the mechanical *energy release rate* G [36, 39, 40] that is equal to the change in total mechanical energy of the body that would occur if the crack were to extend by an increment da . The mechanical energy release rate thus represents the amount of mechanical energy available in the entire body for paying the energetic cost of the dissipative processes. In other words, G provides the energy to drive the crack. The energy release rate G per unit da of crack extension is defined as

$$G = -\frac{d\Pi}{da}, \quad (25)$$

where Π is the total mechanical free energy

$$\Pi = \frac{1}{2} \int_V \sigma_{ij} \epsilon_{ij} dV - \int_S T_i u_i dS. \quad (26)$$

The first term in equation (26) is the elastic energy stored in the loaded body while the second term is the work done by external tractions acting on the boundaries of the body.

There is then a unique relation between the energy release rate G and the stress intensity factor K_I , as shown by Irwin [36, 39], and by Rice [28, 30] using the path independence of the so-called J -integral since the stress and displacement fields depend only on the applied K_I (see equations (9) and (11)). Based on the results presented here, a unique relationship between G and K_I is not immediately obvious. However, for the special case of the center-crack specimen in the isotropic material, with all the fields given in equations (9) and (11), we can explicitly show this relationship. The energy release rate under plane-strain Mode I loading is

$$G = \frac{(1 - \nu)}{2\mu} K_I^2. \quad (27)$$

The fracture criterion $K_I = K_{Ic}$ thus also corresponds to the energetic fracture criterion $G = G_{Ic}$ where G_{Ic} is the energetic cost of the inelastic energy-dissipating processes per increment of crack growth. The fracture toughness K_{Ic} can then be computed from knowledge of the energy cost G_{Ic} due to dissipative processes as

$$K_{Ic} = \sqrt{\frac{2\mu}{1 - \nu} G_c}. \quad (28)$$

The isotropic results of equation (27) can be generalized to full anisotropic elasticity as [37, 41]

$$G = \mathbf{K}^T \mathbf{\Lambda} \mathbf{K}, \quad (29)$$

where $\mathbf{\Lambda}$ is the Stroh energy tensor [41] and $\mathbf{K} = [K_{II}, K_I, K_{III}]^T$ is the stress intensity factor for a mixed mode of loading. We compute the Stroh energy tensor as

$$\mathbf{\Lambda} = \frac{1}{2} \text{Re}(\mathbf{iAB}^{-1}) \quad (30)$$

with \mathbf{A} and \mathbf{B} computed using equation (14).

In a purely brittle material, the energy-dissipating process under quasi-static loading (no dynamics) is solely the creation of new surfaces upon extension of the crack. The critical energy release rate is thus $G_c = 2\gamma_s$ where γ_s is the surface energy of the cleavage plane and

the Mode I fracture toughness is then

$$K_{Ic} = \sqrt{2\gamma_s \Lambda_{22}^{-1}}. \quad (31)$$

Any inelastic process can be characterized by the value of K_I or G at which the process occurs. The subscript c is reserved for the critical process of crack growth. For instance, the critical stress intensity factor for crack-tip dislocation emission in Mode I can be computed. For emission of a dislocation with Burgers vector at an angle ϕ with respect to the crack front direction and occurring along a slip plane at angle θ to the crack plane, the critical Mode I stress intensity for emission is [3, 42]

$$K_{Ie} = \sqrt{G_{Ie} o(\theta, \phi)} / F_{12}(\theta) \cos \phi, \quad (32)$$

where G_{Ie} is a critical energy release rate for dislocation emission, $F_{12}(\theta)$ is a geometrical factor

$$\frac{K_I}{\sqrt{2\pi r}} F_{12}(\theta) = (\sigma_{22} - \sigma_{11}) \sin \theta \cos \theta + \sigma_{12} (\cos^2 \theta - \sin^2 \theta) \quad (33)$$

with σ_{ij} defined by equation (18), and $o(\theta, \phi)$ is an elasticity coefficient given by

$$o(\phi, \theta) = s_i(\phi) \Lambda_{ij}^{(\theta)-1} s_j(\phi) \quad (34)$$

with

$$s(\phi) = (\cos \phi, 0, \sin \phi) \quad (35)$$

and

$$\Lambda_{ij}^{(\theta)} = \Omega_{ik} \Lambda_{kl} \Omega_{jl}. \quad (36)$$

In the last equation Ω is the rotation matrix given by

$$\Omega = \begin{bmatrix} \cos \theta & \sin \theta & 0 \\ -\sin \theta & \cos \theta & 0 \\ 0 & 0 & 1 \end{bmatrix}. \quad (37)$$

The value of G_{Ie} for emission is not known *a priori*, and must be estimated based on theoretical analyses of the emission process. A recent theory that includes the energy costs associated with both creation of a critical amount of slip along the emitting slip plane and the surface step formed at the crack tip has been shown to accurately capture a wide range of atomistic simulations in fcc materials [43]. A simplified analytic result for G_{Ie} emerging from that study is

$$G_{Ie} = \begin{cases} 0.145\gamma_s^e + 0.5\gamma_{\text{usf}} & \gamma_s^e > 3.45\gamma_{\text{usf}} \\ \gamma_{\text{usf}} & \gamma_s^e < 3.45\gamma_{\text{usf}} \end{cases}, \quad (38)$$

where γ_{usf} is the unstable stacking fault energy for slip along the slip plane and γ_s^e is the surface energy for the emission plane.

The two cases above, brittle failure and dislocation emission, are important because they establish the intrinsic ductility of a crystalline material. A material is *intrinsically ductile* if $K_{Ie} < K_{Ic}$ (dislocation emission precedes fracture) and is *intrinsically brittle* if $K_{Ic} < K_{Ie}$ (brittle cleavage precedes dislocation emission). In section 4 we analyze the competition between Griffith cleavage and crack-tip dislocation emission to elucidate important issues in the atomistic modeling of fracture.

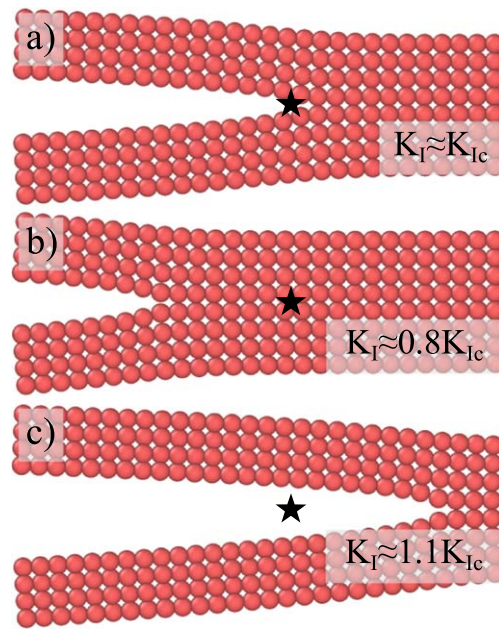


Figure 3. Closing and opening of an atomically sharp crack when the applied K_I is below and above the Griffith value, respectively. Atoms are visualized using OVITO [54].

3. Simulation methods and issues

3.1. Creating cracks in atomistic systems

The LEFM-envisioned crack, as a slit of zero elastic modulus consisting of upper and lower *traction free crack surfaces*, often cannot be created naturally in atomistic simulations. A traction free condition cannot be simply imposed on atoms due to atomic interactions across the crack surfaces. As a consequence, an atomically sharp crack is unstable to closure at loads below the Griffith K_{Ic} , or it is unstable to propagation at loads above the K_{Ic} . However, in extremely brittle materials (no crack-tip dislocation emission prior to cleavage), it is possible to simulate an atomically sharp and stable crack at $K_{Ic} \pm \Delta K$ with ΔK being very small but having some finite value [11, 44–46]. Stability of the crack at loads $\sim K_{Ic}$ is due to effect known as ‘lattice trapping’ [6, 47]. This effect arises because of the discrete nature of an atomic system in which precise force law, that characterizes atomic interactions, can restrain crack opening until the crack tip bond is mechanically unstable. At this point, the applied stress intensity factor exceeds the thermodynamic Griffith value K_{Ic} . Similarly, in the case of unloading, the applied load for crack to close falls behind the Griffith K_{Ic} . The lattice trapping is usually very small in metals, where the critical stress intensity for crack to grow is only few percents above K_{Ic} . However, it can be considerably larger in materials such as silicon [45, 48]. The crack stability as a function of the applied K_I has been examined explicitly using atomistic simulations and the K -test geometry in fcc Ni [49] (see figure 3).

For describing the intrinsic nature (intrinsic ductility/brittleness) of a material we usually explore some competitive crack-tip processes that occur at loads below Griffith K_{Ic} . Therefore, to prevent the crack from closure we have to use one of the following approximate methods for creating a traction free crack:

- (i) ‘Screening’, where we artificially delete interactions between atoms on either side of the initial crack surfaces. However, since interatomic potentials are typically multibody (long-range), the screening can slightly change the behavior of all the atoms at/near the crack tip.
- (ii) ‘Blunting’, where we delete a few layers of atoms to create crack surfaces. The finite distance between the crack surfaces prevents atomistic interactions across the crack faces and leads to the desired traction free condition. However, a slightly blunted crack is created and so deviations from the ideally sharp crack can arise (the crack-tip singularity is removed).

The quantitative difference between a truly sharp crack, ‘screening’, and ‘blunting’ will be explored in section 4.1.2.

3.2. Center-crack and other finite-crack geometries

Simulations using finite-size cracks appear convenient—they are easy to construct, the loading is simple, and the geometries are similar to macroscopic test specimens. Thus, the results from fracture mechanics are thus often used for interpretation without detailed investigation of the applicability of LEFM. Here, we highlight a few of the general issues that make these finite-size crack tests undesirable for atomistic simulations.

We emphasize the conditions for a valid transferable measure of crack tip fracture processes: $r_{\text{FPZ}} \ll r_K \ll a$. The size of r_{FPZ} for a sharp crack can be estimated using the non-linear/non-convex energy versus separation curve obtained from the separation of two rigid blocks of material starting from the zero-stress equilibrium configuration [50]. This traction separation curve often follows the so-called universal Binding energy curve [51]. Approximating the actual curve by the Dugdale model of a constant cohesive stress σ_c acting over a maximum crack opening of δ yields the fundamental cohesive length $\delta_c \approx 3E\delta/8\sigma_c$ [52, 53], and $\delta_c \approx r_{\text{FPZ}}$. With the typical ratio $\sigma_c/E = 1/10$ and maximum opening $\delta \approx a_0/5$, the cohesive length is $\delta_c \sim a_0$. Thus, the minimum crack size to satisfy $r_{\text{FPZ}} \ll r_K \ll a$ with $r_{\text{FPZ}} = a_0$, $r_K = 2r_{\text{FPZ}}$, and $r_K = 0.15a$, is $2a = 26a_0 \approx 100 \text{ \AA}$. A total system size should usually be $10\times$ larger to avoid boundary effects. Plane-strain simulations at this scale ($1000 \text{ \AA} \times 1000 \text{ \AA} \times a_0$) involve approximately 360 000 atoms and are computationally quite feasible. However, this scale is at the absolute minimum level and only satisfies one general requirement of LEFM.

For more complex problems, much larger cracks are necessary to ensure K -dominance. For instance, a crack along a grain boundary has an intrinsic scale associated with the periodic length of the grain boundary structure l_{gb} . Even for relatively simple grain boundaries, this structure has a length of multiple lattice constants. Study of fracture along or near a grain boundary then requires that at least a length l_{gb} exist within the K -dominant region, so $l_{gb} < r_K$ sets an absolute minimum on r_K and hence the allowable crack size a and, consequently a minimum total system size. Again, cracks at this scale can be simulated, but the problems become computationally more demanding and with many atoms in the non-asymptotic domain.

A more serious problem is that the applied stress levels needed to drive crack tip phenomena are very high in finite-crack specimens. The applied stress necessary to generate a stress intensity K_I is $\sigma^{\text{app}} = K_I/\sqrt{\pi a}$. Taking a typical stress intensity factor at which crack-tip phenomena arise as $K_I = 1 \text{ MPa } \sqrt{\text{m}}$, the applied stress versus crack length is shown in figure 4. These stress levels are on the order of 1–15 GPa for cracks up to $a \approx 320 \text{ nm}$. At this

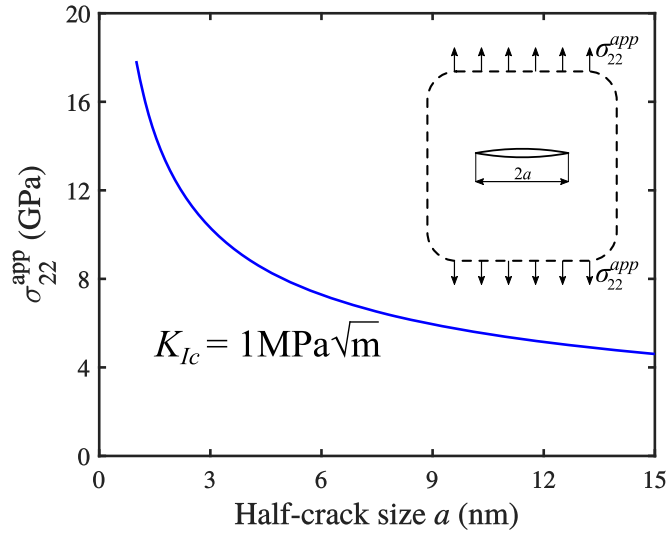


Figure 4. Far-field applied stress at the cleavage point with $K_{Ic} = 1 \text{ MPa} \sqrt{\text{m}}$, as a function of the half crack size a .

magnitude of the far-field stresses, the stresses in the non-asymptotic region are at this level or larger, and this creates two severe problems.

The first problem is that the entire material is no longer linearly elastic, violating the basic premise of LEFM. Figure 5 shows the tangent elastic moduli for single crystal Ni using the well-established Mishin EAM potential for Ni [49]. Computational details are presented in the [appendix](#). The elastic constants vary notably at high stresses, so that predictions based on LEFM become invalid. Often, simulations are performed with applied displacements rather than stresses, with the stresses computed from linear elasticity and then used in LEFM to determine the operative K_I in the simulation. Such simulations can be partially corrected by using the measured stress, but the entire material is still behaving nonlinearly and so care must be taken in subsequent application of LEFM (although some aspects of LEFM are preserved for nonlinear (hyper-) elastic materials).

The second problem is that the high stresses well ahead of the crack drive nonlinear/inelastic/damage phenomena that are outside the intended FPZ. Conversely, these high stresses create an FPZ that has $r_{\text{FPZ}} > r_K$, violating LEFM. This can be especially problematic for the study of crack/defect interactions, because the defects can respond to the high non-asymptotic stress fields while still far ahead of the crack, initiating processes that would not occur until much higher load levels or for defects only much closer to the crack tip. Study of grain boundaries is particularly prone to this problem, since grain boundaries can emit dislocations at stresses well below the cohesive strength of the material. Thus, in finite-crack specimens, grain boundary emission may occur unrealistically far ahead of the crack. The study of dislocation/crack interactions is another case where the high stresses are problematic. The Peierls stress for a dislocation is often rather low (1–100 MPa, especially in fcc metals and alloys, and some hcp slip systems). Thus, dislocations near the crack tip can move very far from the crack—outside of r_K due to the high far-field stresses. Dislocations can also be driven toward the crack by the same high stresses. In both cases, the dislocations are moving in response to fields generated by the specimen geometry, and not solely by the crack tip field. We will show this explicitly below.

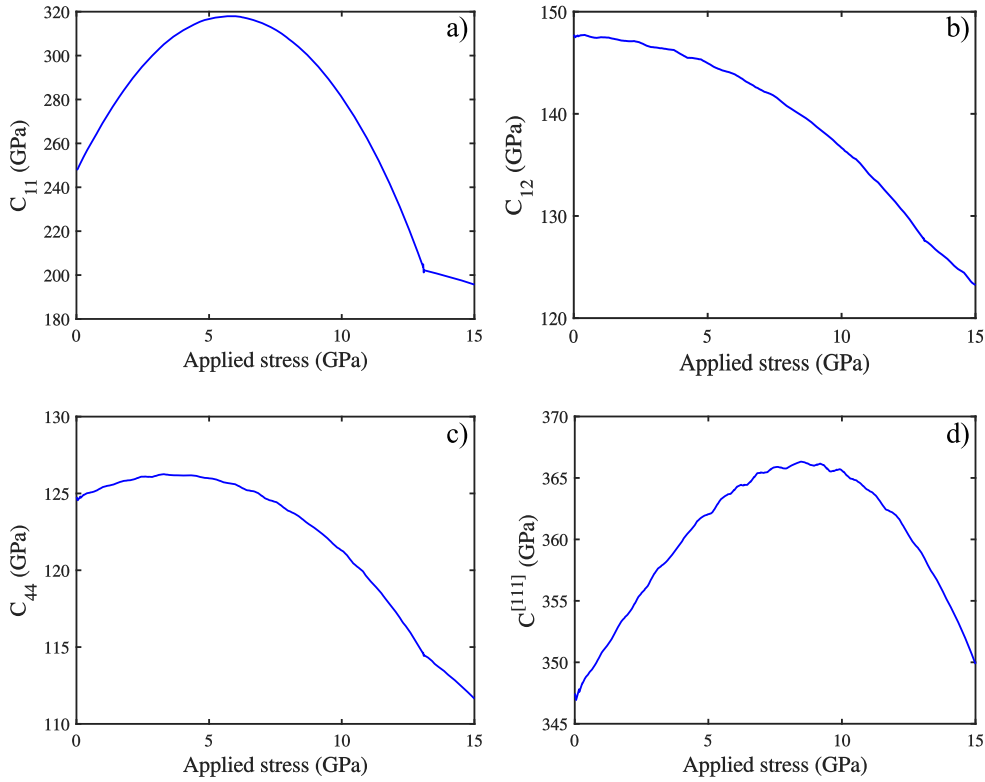


Figure 5. Elastic constants as a function of the applied normal stress in fcc nickel.

3.3. *K*-controlled simulation framework

We have highlighted the importance of maintaining the length scale hierarchy $r_{\text{FPZ}} \ll r_K \ll a$ and some of the challenges in doing so within the center-crack specimen, which extends to any other finite-crack test specimens. These challenges can be entirely circumvented by using a different test geometry corresponding to a semi-infinite crack. The *K*-controlled geometry forgoes modeling of an entire finite specimen and instead explicitly studies only the asymptotic crack tip region. Specifically, a simulation cell is created in which an edge crack (traction free surface) extends in toward the middle of the specimen. The boundary conditions on all outer cell boundaries are the displacement fields of the asymptotic near-crack fields of equations (11), (13) or (19) (depending on materials anisotropy and symmetry) with respect to the crack tip position. By construction, the entire simulation domain is then within the asymptotic *K*-field. The loading parameter is then precisely K_I (and can be extended to include K_{II} and K_{III}). The response of the material is then also precisely the intrinsic crack tip response under the stress intensity loading.

In this *K*-test geometry, there is no crack size; a is essentially infinite. The entire specimen is within the *K*-dominant zone by construction. The only requirement for a valid fracture test is then that $r_{\text{FPZ}} \ll r_{\text{sim}}$ where r_{sim} is a characteristic simulation cell radius (although the cell can be of any shape). For the same total number of atoms in a simulation cell, the *K*-test geometry ensures that all the atoms are within the *K*-dominant zone and maximizes the number of atoms in the FPZ. Furthermore, the simulation cell size needed is

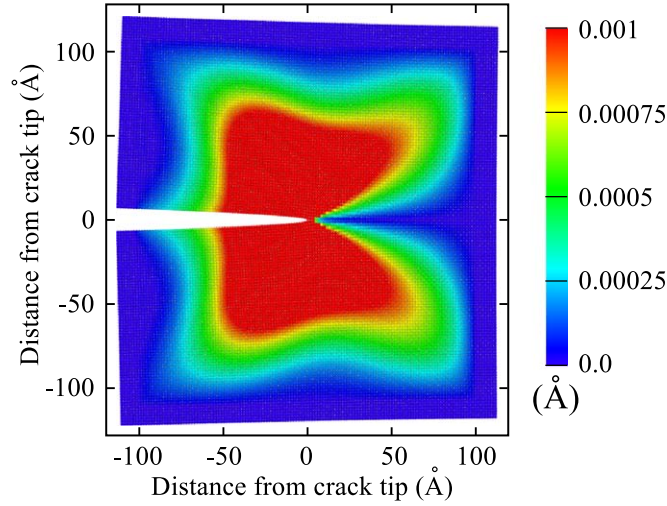


Figure 6. Absolute difference in x_2 atomic positions between the elastic solution given by equation (19) (K -field) and relaxed structure for the same applied K_I within the box size of $21 \times 21 \times 1 \text{ nm}^2$. Atoms are colored according to x_2 displacement difference shown by the scale. Displacement difference in the red zone is off-scale with maximum displacement of 0.012 Å .

determined entirely by the FPZ of the process under study, and can be quite small for phenomena that are highly localized to the crack tip. These assumptions have been verified explicitly via simulations; other specific details are presented in section 4.1. Figure 6 shows the absolute displacement difference $\Delta u_2 = |u_2 - u_2^{\text{relaxed}}|$ computed in fcc Ni [49] at the applied $K_I = 0.85 \text{ MPa}\sqrt{\text{m}}$, where u_2 is the elastic solution given by equation (19), while u_2^{relaxed} are atomic positions after energy minimization is performed. The nonlinear atomic displacements, generated during the energy minimization, are present only in the zone close to the tip (FPZ). We find $\Delta u > 0.005 \text{ Å}$ within the radius of $\sim 2 \text{ nm}$, and $\Delta u > 0.001 \text{ Å}$ within the radius of $\sim 10 \text{ nm}$, around the crack tip. The maximum displacement difference is at the tip with the magnitude $\Delta u = 0.012 \text{ Å}$. Atoms outside the FPZ thus preserve their elastic positions as given by equation (19) (K -dominance zone) although they are allowed to move freely. Thus, the ‘ K -test’ completely satisfies the concept of LEFM. Unlike the finite-crack specimens, the stress fields are the correct asymptotic fields and there are no artificially high stresses far ahead of the crack tip. All defects inside the simulation domain thus also experience the correct stress fields.

There are very few disadvantages to the K -test geometry. One disadvantage is the need for the correct asymptotic displacement fields in complex problems. For instance, for a sample with a grain boundary where the crystalline material is elastically anisotropic, the single-crystal anisotropic fields are not appropriate. Anisotropic solutions can be created for some geometries, especially with reflection symmetry across the crack plane, but there are no general solutions. In contrast, a CCT specimen does not require imposition of any displacement boundary conditions and so the consequences of the change in crystalline orientation across the grain boundary are automatically incorporated. However, the CCT specimen remains problematic for other reasons. Another apparent disadvantage of the K -test is that the boundary conditions are specific to the position of the crack tip so that the boundary conditions become inaccurate as the crack extends. This issue is, however, easily rectified by

updating the crack tip position as the simulation proceeds so that the boundary conditions always correspond to the actual crack tip position (see section 4.3).

The K -test geometry has been used for decades in continuum-level finite element simulations of fracture problems. It has been employed precisely to maintain SSY conditions at all times. Its adoption in atomistic simulations has, unfortunately, been more sporadic.

4. Illustrative examples

In the following sub-sections, we analyze several basic fracture problems using molecular statics and dynamics simulations at $T = 0$ K to highlight the general points made above. For each of the first few problems, we use single-crystal Ni as the test material and examine both the K -test and CCT test geometries, examine convergence, and compare them against one another and against theoretical predictions. In the final problem, we examine fracture processes and crack growth in an amorphous material in the K -test and highlight key features. Simulations are executed using the large-scale atomistic/molecular massively parallel simulator [55]. Key material properties computed with the Ni EAM interatomic potential [49] are shown in table 1. The fcc elastic properties reveal a Zener anisotropy of $A = 2C_{44}/(C_{11} - C_{12}) = 2.5$ ($A = 1$ for isotropy) and so we use anisotropic analyses to set boundary conditions in the K -test and also use equation (31) to compute K_{Ic} for Griffith cleavage and equation (32) to compute K_{Ic} for crack-tip dislocation emission (see table 1). We then examine fracture in the amorphous Li-Si system, with the Li and Si interactions described by a reasonable MEAM potential [56].

4.1. Brittle fracture

4.1.1. Brittle fracture: simulation set-up. As the first illustrative example we analyze brittle fracture in fcc Ni single crystal under plane strain loading conditions. A minimum requirement for simulating Griffith cleavage, as already discussed in section 2.5, is $K_{Ic} < K_{Ie}$. To achieve this condition, we use a single crystal oriented with $X_1 = [1\ 0\ 0]$, $X_2 = [0\ 1\ 0]$ and $X_3 = [0\ 0\ 1]$ for which, by using material properties presented in table 1 and equation (31), we compute $K_{Ic} = 0.91\text{ MPa}\sqrt{\text{m}}$. The crack front then intersects an oblique $\langle 1\ 1\ 1 \rangle$ slip plane making dislocation emission to difficult ($K_{Ic} \ll K_{Ie}$); therefore, we do not show K_{Ie} . We further present specific simulation details that have not been discussed in sections 3.2 and 3.3. In both test geometries, the crack is lying in the x_1 - x_3 plane with crack front along x_3 . Periodic boundary conditions are applied along x_3 while traction free boundaries are imposed in x_1 and x_2 directions. Since the simulations are performed in a homogeneous material at $T = 0$ K, results are independent of cell thickness in x_3 direction; therefore, for both test geometries we set the simulation cell thickness to be ~ 1 nm.

In the K -test geometry (see figure 7(a)), the simulated crack tip of a semi-infinite crack is at $x_1 = 0$ and $x_2 = 0$, and the cell size has dimensions of approximately $120 \times 120\text{ nm}^2$ in x_1 - x_2 plane. We perform three different simulations using cracks created by the three possible methods: truly sharp crack, screening, and blunting (see section 3.1). Since the $[001]$ is one of the mirror planes in fcc metals, we load the crack corresponding to the applied K_I by imposing atomic displacements using equation (19). After each loading increment of $\Delta K = 0.01\text{ MPa}\sqrt{\text{m}}$, atoms within $2r_c$ (r_c = cut-off distance of the interatomic potential) of the simulation outer boundary are held fixed (see figure 7), while all other atoms are relaxed to minimize the total energy of the system using the ‘fire’ method [57] with the force tolerance of $10^{-6}\text{ eV}\text{ \AA}^{-1}$ on every atom. However, within the material studied here we find no difference in the simulated results with the force tolerance of 10^{-5} and $10^{-4}\text{ eV}\text{ \AA}^{-1}$ on

Table 1. Material properties of fcc Ni used to compute its critical stress intensity factors for Griffith cleavage K_{Ic} (equation (31)) and dislocation emission K_{Ie} (equation (32)). Model orientations are defined by the crack plane normal (\mathbf{n}), and the crack front direction [I].

a_0 (Å)	C_{11} (GPa)	C_{12} (GPa)	C_{44} (GPa)	γ_{usf} (J m ⁻²)	γ_{utf} (J m ⁻²)	$\gamma_s^{[100]}$ (J m ⁻²)	$\gamma_s^{[111]}$ (J m ⁻²)	K_{Ic} (010)[001] (MPa \sqrt{m})	K_{Ic} (111)[$\bar{1}10$] (MPa \sqrt{m})	K_{Ie} (111)[$\bar{1}10$] (MPa \sqrt{m})
3.52	247.9	147.8	124.8	0.367	0.428	1.882	1.631	0.91	0.92	0.80

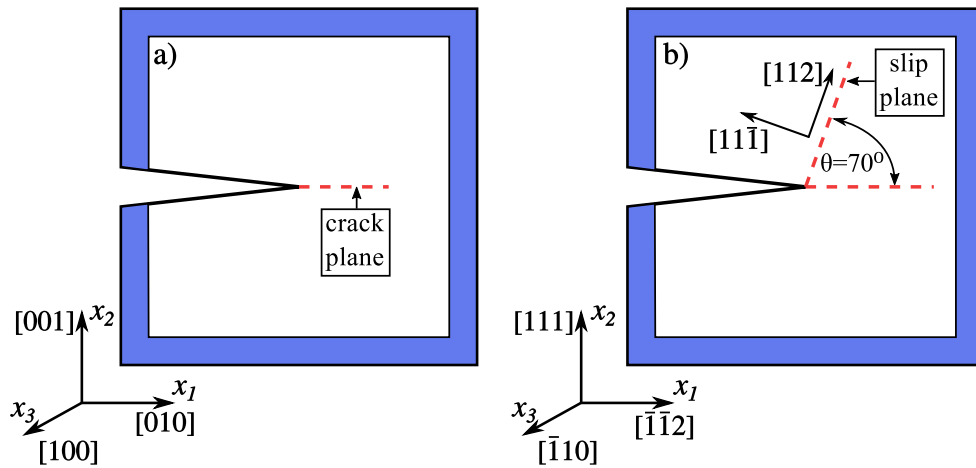


Figure 7. *K*-test geometry used to simulate (a) brittle fracture and (b) dislocation emission from the crack-tip. Blue color indicate domain of atoms where boundary conditions are applied.

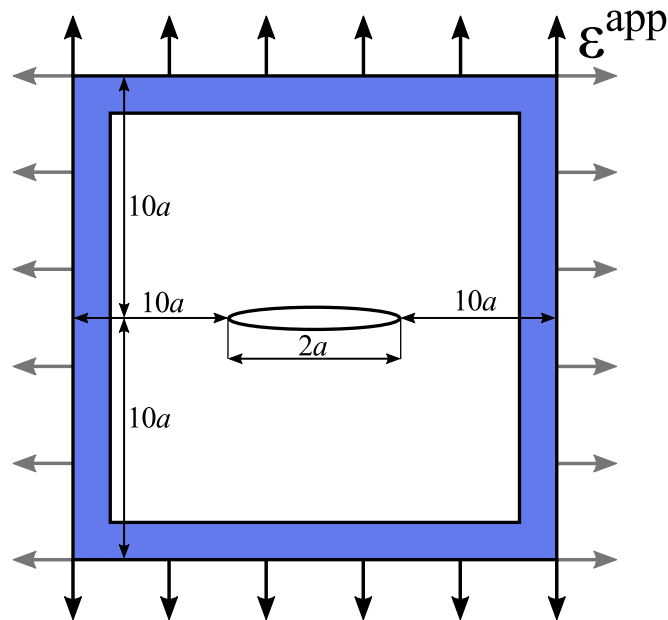


Figure 8. CCT test geometry used to simulate centrally positioned finite crack under uniaxial (only black arrows) or biaxial (black and gray arrows) applied strain ϵ^{app} . Blue color indicates domain of atoms where boundary conditions are applied.

every atom. This is not a surprising since the crack-tip stresses are on the order of several GPa before any interesting event occurs. The simulation is terminated once the crack starts to propagate.

In the CCT test geometry (see figure 8), we simulate a centrally positioned crack having a finite size $2a$ with two tips at $x_1 = \pm a$ and $x_2 = 0$. The simulation box has size of $22a \times 20a$

in the x_1-x_2 plane. To investigate the effects of size and nonlinearity we vary the half crack size a approximately between 2 and 15 nm. We analyze both uniaxial and biaxial loading using displacement boundary conditions. After each loading increment of $\Delta\epsilon^{\text{app}} = 0.001$, the boundary atoms within $2r_c$ of the simulation cell outer boundary are held fixed at the imposed displacement corresponding to the applied strain ϵ^{app} while all other atoms are relaxed to minimize the total energy of the system using the fire method [57]. Since we need to simulate several million atoms for $a > 5$ nm we use a force tolerance of 10^{-5} eV \AA^{-1} in biaxial tension and 10^{-4} eV \AA^{-1} in uniaxial tension. We terminate the simulation when cleavage begins. We compute K_{Ic} for the slit crack using $K_{\text{Ic}} = \sigma_{22}^{\text{cr}} \sqrt{\pi a}$, where the critical applied stress σ_{22}^{cr} corresponds to the critical applied strain ϵ^{cr} , and is computed either (i) directly from simulations $\sigma_{22}^{\text{cr}} = \sigma_{22}^{\text{cr, sim}}$, or (ii) from Hooke's law $\sigma_{22}^{\text{cr}} = C_{22ij} \epsilon_{ij}^{\text{cr}}$. A traction free crack is formed using 'screening.'

4.1.2. Brittle fracture: simulation results. The observed crack tip behavior in both the K -test and the CCT test geometries is cleavage, as planned. We now focus on quantitative results observed using the K -test geometry. The simulated critical stress intensity factor for Griffith cleavage is $K_{\text{Ic}} = 0.93 \text{ MPa } \sqrt{\text{m}}$ when the truly sharp crack configuration is used, and $K_{\text{Ic}} = 0.92 \text{ MPa } \sqrt{\text{m}}$ when 'screening' is used. A slightly lower K_{Ic} in 'screening' arises due to deletion of atomic interactions across the crack surfaces that affects the response of the crack-tip atoms. However, both simulated K_{Ic} values are only slightly higher than the K_{Ic} predicted by LEFM (see table 1). This is expected due to small lattice trapping, as discussed in section 3.1. We further examine the simulated behavior when the crack is formed by deletion of two, three and four atomic layers, respectively (see figure 9). In every case we find a considerable increase in K_{Ic} since the 'blunting' changes the singularity at the tip [8]. The lowest K_{Ic} is obtained for a crack formed by deletion of three atomic layers because this configuration preserves the morphology that most closely resembles the sharp crack (see figure 9(b)). Note that the distinct steps and the void in figures 9(c)(2) and (c)(3) are generated by the nonlinear atomic rearrangements and not due to dislocation activity. Using 'blunting' for crack formation is useful since the crack tip can be blunted by different real physical processes that may occur at the atomic scale. However, soon after the crack starts to propagate, its growth is mainly controlled by the condition for a truly sharp crack. Thus, the sharp crack should always be considered as a fundamental starting point in evaluation of intrinsic brittleness/ductility.

We next investigate the influence of the simulation cell size on fracture toughness using the truly sharp crack configuration. For the material considered here we find that a cell size of $21 \times 21 \times 1 \text{ nm}^3$, with the crack tip ~ 10 nm far from the boundary, is sufficiently for converged results (see figure 10). Decreasing the simulation cell size leads to only a modest increase in simulated K_{Ic} . This is expected because the nonlinear/non-convex atomic behavior (the FPZ) exists only in the crack tip vicinity, as discussed above (see figure 6). Overall, the K -test geometry is shown to be, quantitatively and qualitatively, a very well-controlled model for simulating brittle fracture at atomic scale.

We now explore results obtained using the CCT test geometry under uniaxial and biaxial tension. Figure 11 shows the critical stress intensity factor for cleavage computed as $K_{\text{Ic}} = \sigma_{22}^{\text{cr}} \sqrt{\pi a}$. The σ_{22}^{cr} is obtained from the measured critical applied strain $\epsilon_{ij}^{\text{cr}}$ in two ways. First, we use Hooke's law $\sigma_{22}^{\text{cr}} = C_{22ij} \epsilon_{ij}^{\text{cr}}$ with the small-strain elastic constants. Second, we use the measured stress in the simulation, $\sigma_{22}^{\text{cr}} = \sigma_{22}^{\text{cr, sim}}$ computed from the average virial stress of the entire atomic system in x_2 direction; this method is commonly used in the vast literature publish to date. However, this method for evaluating $\sigma_{22}^{\text{cr, sim}}$ can introduce some

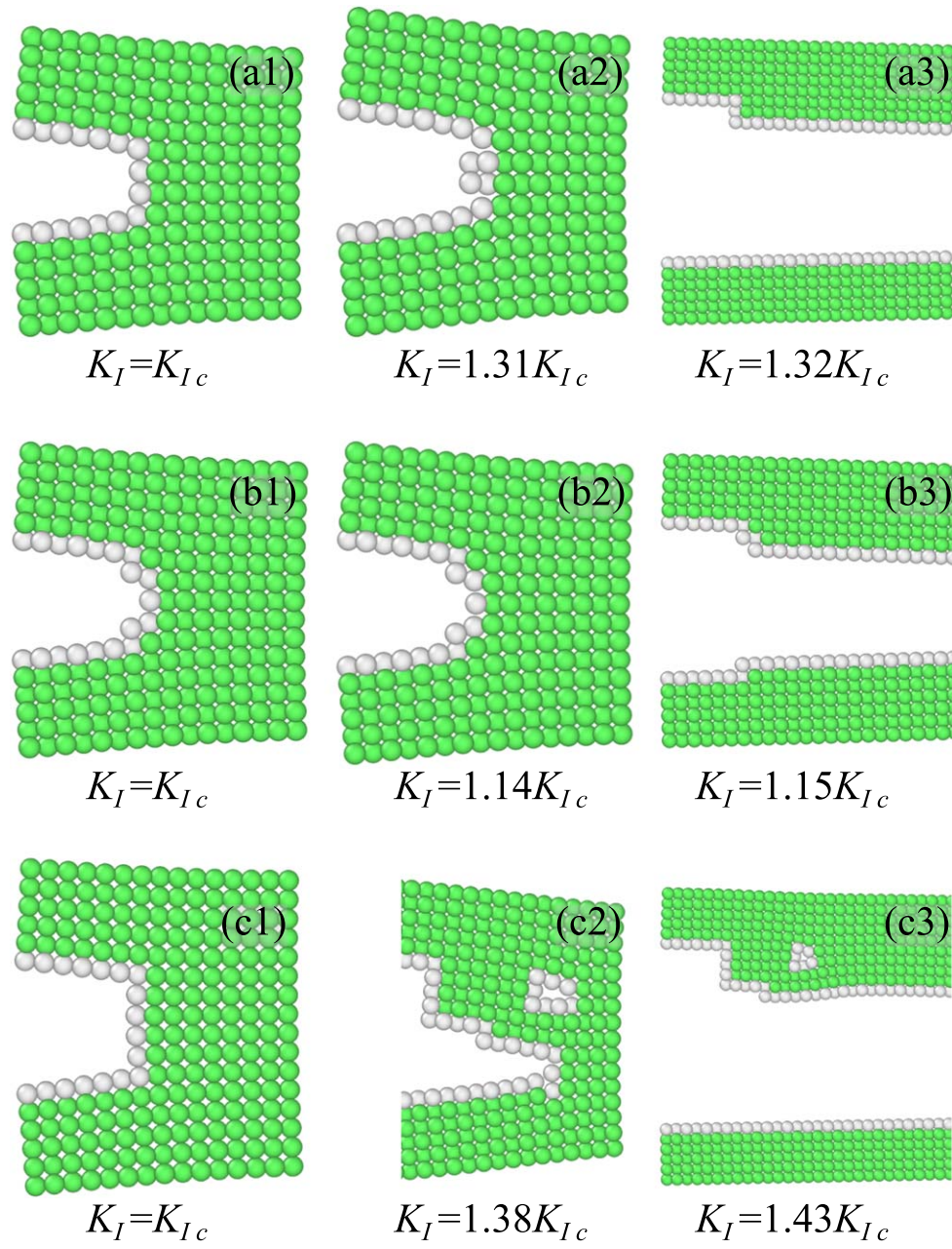


Figure 9. K -test geometry for blunted cracks created by deletion of (a) two, (b) three and (c) four atomic layers. In each case, the left figure shows the crack tip morphology at the applied $K_I = K_{Ic} = 0.91 \text{ MPa } \sqrt{\text{m}}$, the middle figure shows the crack tip at the applied K_I immediately before the cleavage, while the right figure shows the crack after brittle fracture started. Atoms in this figure are colored based on common neighbor analysis [54]; green for fcc and white for surface.

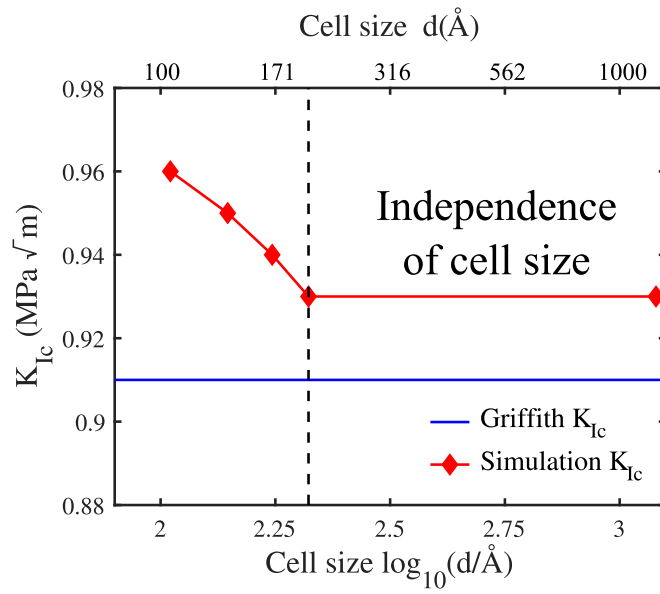


Figure 10. Critical stress intensity factor for cleavage K_{Ic} as observed in the K-test simulations for different simulation cell sizes (red diamonds), along with the predictions of LEFM based theoretical prediction (equation (31)) (blue line). The black dashed line represents minimum cell size for converged results.

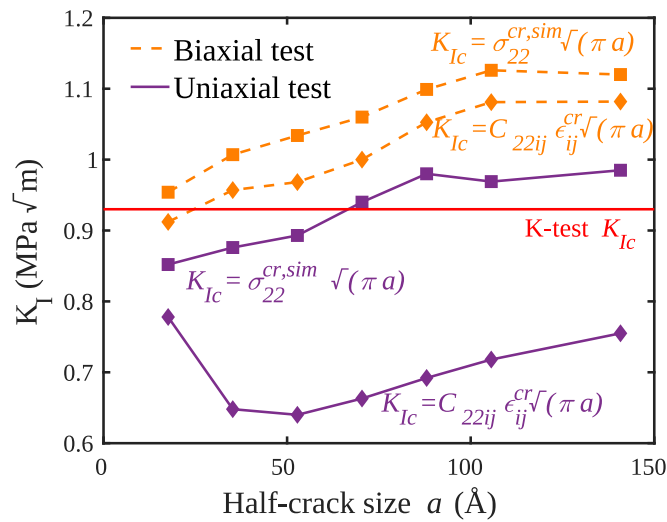


Figure 11. Computed critical stress intensity factor for cleavage $K_{Ic} = \sigma_{22}^{cr} \sqrt{\pi a}$ versus crack size a in the CCT test simulations (see figure 8) under uniaxial (purple solid lines) and biaxial (orange dashed lines) loading. Squares correspond to results computed using σ_{22}^{cr} directly from simulations while diamonds corresponds to results computed using $\sigma_{22}^{cr} = C_{22ij} \epsilon_{ij}^{cr}$. Solid red line: K-test result.

uncontrolled errors which mainly arise due to nonlinear behavior and elastic relaxations. A more precise method for estimating $\sigma_{22}^{\text{cr, sim}}$ is to use the same simulation cell without a crack but loaded at the same critical applied strain ϵ^{cr} . In addition, for comparison, figure 11 shows the converged K -test simulation results obtained using the truly sharp crack. Note that we do not compare the simulated results with the Griffith value for K_{Ic} since the nanoscale CCT test geometry violates the basic concept of LEFM (see below). Several crucial features emerge from figure 11. First, the deduced K_{Ic} varies with crack size a . This result should immediately preclude any further application of the nanoscale CCT test since K_{Ic} is a material property independent of the crack size. Second, the estimated K_{Ic} is either far above or far below the K -test result, with no tendency toward convergence with increasing a . Third, since the elastic moduli increase with applied stress (see figure 5), the computed K_{Ic} is higher when σ_{22}^{cr} is used directly from simulations. Finally, the simulated K_{Ic} depends on whether we apply biaxial or uniaxial tension, even though σ_{11}^{app} does not contribute to the crack-tip singularity. All these differences arise due to (i) material nonlinearity associated with extremely high applied stresses, and (ii) violation of the length scale hierarchy $r_{\text{FPZ}} \ll r_k \ll a$ (see section 2.3). The above results clearly confirm our previous conclusions that atomistic simulation of a finite size crack are not a reliable approach for obtaining quantitative insights into material fracture characteristics at the nanoscale.

4.2. Crack-tip dislocation emission

4.2.1. First partial dislocation emission. As the second illustrative example we analyze dislocation emission from the crack-tip using both the K -test and CCT test geometries again. A fundamental requirement for observing the emission is $K_{\text{Ie}} < K_{\text{Ic}}$. To achieve this, we orient the crystal with $X_1 = [\bar{1} \bar{1} 2]$, $X_2 = [1 1 1]$ and $X_3 = [\bar{1} 1 0]$, forming a crack with a single $(11\bar{1})$ slip plane inclined at the angle $\theta = 70.53^\circ$ to the crack. Using this orientation, material properties presented in table 1, and equations (31) and (32), we compute $K_{\text{Ie}} = 0.80 \text{ MPa } \sqrt{\text{m}}$ and $K_{\text{Ic}} = 0.92 \text{ MPa } \sqrt{\text{m}}$, satisfying the condition for intrinsic ductility. One of the approximate methods for creating traction free crack surfaces must now be used since emission should occur at a load below the Griffith K_{Ic} (see section 3.1) where the sharp crack would be closing from the start of the simulation [58]. In the K -test geometry we use both ‘screening’ and ‘blunting’ by deletion of three atomic layers while in the CCT test geometry we only use ‘screening’. All other simulation details are as presented in section 4.1.1.

The observed crack tip event in both geometries studied here is the emission of a partial dislocation prior to Griffith cleavage. We again first discuss results observed in the K -test simulations. The simulated critical stress intensity factor for crack tip dislocation emission, for both ‘screening’ and ‘blunting’, is $K_{\text{Ie}} = 0.77 \text{ MPa } \sqrt{\text{m}}$. While for the material studied here we find no difference between ‘screening’ and ‘blunting’, in the majority of other materials studied we find ‘screening’ better represents the truly sharp crack [43]. Therefore, we only use ‘screening’ for all subsequent studies. More details on how crack formation affects dislocation emission can be found in [43]. The theoretical predictions computed using equations (32) and (38) are slightly higher than the simulations (see table 1) but the agreement remains very good. The difference arises because the theory assumes existence of nonlinear slip only along a single slip plane while in reality there is some other nonlinear behavior around the crack tip. Similarly to the brittle fracture, a simulation cell size of $18 \times 18 \text{ nm}^2$ is sufficient for converged results (see figure 12). Overall, the K -test geometry is again shown to be an accurate and computationally-efficient method for simulating the crack-tip dislocation emission.

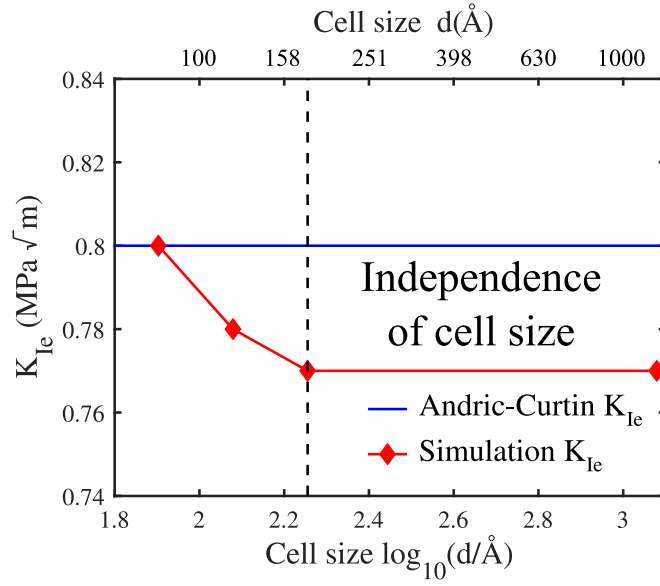


Figure 12. Critical stress intensity factor for crack-tip dislocation emission K_{Ie} as observed in the K -test simulations for different simulation cell sizes (red diamonds), along with the predictions of LEFM based theoretical prediction (equation (38)) (blue line). The black dashed line represents minimum cell size for converged results.

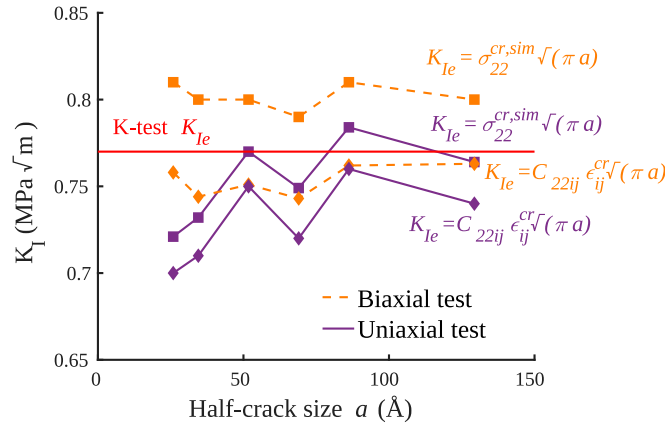


Figure 13. Computed critical stress intensity factor for crack-tip dislocation emission $K_{Ie} = \sigma_{22}^{cr} \sqrt{\pi a}$ versus crack size a in the CCT test simulations under uniaxial (purple solid lines) and biaxial (orange dashed lines) loading. Squares correspond to result computed using σ_{22}^{cr} directly from simulations while diamonds correspond to results computed using $\sigma_{22}^{cr} = C_{22ij} \epsilon_{ij}^{cr}$. Solid red line: K -test results.

We now show results on crack tip dislocation emission observed using the CCT test geometry. Figure 13 shows K_{Ie} , computed using both $K_{Ie} = \sigma_{22}^{cr, sim} \sqrt{\pi a}$ and $K_{Ie} = C_{22ij} \epsilon_{ij}^{cr} \sqrt{\pi a}$, in uniaxial and biaxial tension tests. The converged K -test result is also shown. Once again we find a dependence of K_{Ie} on the crack size, loading scenario, and

method used to evaluate σ_{22}^{cr} . However, the quantitative difference between the K -test and CCT test geometries, especially in biaxial tension, is smaller for dislocation emission than in brittle fracture. The fairly good agreement between the two test geometries is due to the smaller nonlinear behavior of the crystal oriented with (111)[$\bar{1}10$] (see figure 5(d)) and the lower applied stresses. However, the material response versus applied stress is not known *a priori* unless specifically measured in advance.

4.2.2. Dislocation/crack interaction: equilibrium position of the first partial dislocation. After nucleation, the first partial dislocation moves to an equilibrium distance r along the slip plane ahead of the crack, at which point the total Peach–Koehler (P–K) force is zero [3]. For a partial dislocation emitted from a semi-infinite crack, the total P–K force has the following form

$$\frac{K_I F_{12}(\theta) b_p}{\sqrt{2\pi r}} - \gamma_{\text{ssf}} - \frac{b_p^2 o(\theta, \phi)}{8\pi r} = 0, \quad (39)$$

where b_p is the partial dislocation Burgers vector, and γ_{ssf} is the stable stacking fault energy. The three terms in this equation are (i) the force due to the applied K_I , resolved for a particular slip plane inclination angle, that moves the dislocation away from the crack tip, (ii) the stacking fault that drives dislocation back toward the tip, and (iii) the image force due to crack free surface, which also attracts the dislocation back toward the crack tip. We neglect the intrinsic Peierls stress of the partial dislocation moving through the lattice because it is small. A simple manipulation yields the equilibrium distance r as a function of the applied K_I given by

$$r = \frac{(K_I F_{12}(\theta))^2 b_p^2}{8\pi \gamma_{\text{ssf}}^2} \left(1 + \sqrt{1 - \frac{\gamma_{\text{ssf}} o(\theta, \phi)}{(K_I F_{12}(\theta))^2}} \right)^2, \quad (40)$$

where the exact solution is the largest root. The preceding equation is valid in an infinite medium. In a finite size cell there is an additional contribution to the P–K force due to the fixed boundary that repels the dislocation from the boundary back toward the tip. The boundary effect on r has been evaluated explicitly using atomistic simulations in the K -test geometry. Figure 14(a) shows the equilibrium position of the first partial dislocation immediately after nucleation using different simulation cell sizes. While the difference between equation (40) and simulated r is rather small in the largest simulation cell, a considerable difference emerges with decreasing cell size. The importance of this distance between the dislocation(s) (far-field plasticity) and the crack-tip is discussed in the following section.

We next examine the equilibrium position of the first partial dislocation simulated in the CCT test geometry. The problematic contribution of the high far-field stress to the equilibrium distance can be easily assessed by comparing results in uniaxial and biaxial tension. Neglecting the contribution of the asymptotic crack-tip field, and recalling that the resolved shear stress along the slip plane inclined at an angle θ is $\tau_r(\theta) = (\sigma_{22}^{\text{app}} - \sigma_{11}^{\text{app}}) \sin\theta \cos\theta + \sigma_{12}^{\text{app}} (\cos^2\theta - \sin^2\theta)$, we expect that the equilibrium distance r of the first partial dislocation to be much larger in uniaxial tension. This is shown clearly in figure 14(b). Due to the very low Peierls stress for dislocations in fcc metals, the first partial dislocation under uniaxial loading always moves nearly to the simulation cell boundary. The asymptotic crack tip stress field does not contribute to the final position r in the CCT test under uniaxial tension. Instead, the dislocation position is controlled by the non-asymptotic stress field. In biaxial tension the far-field resolved shear stress along the slip plane is effectively zero.

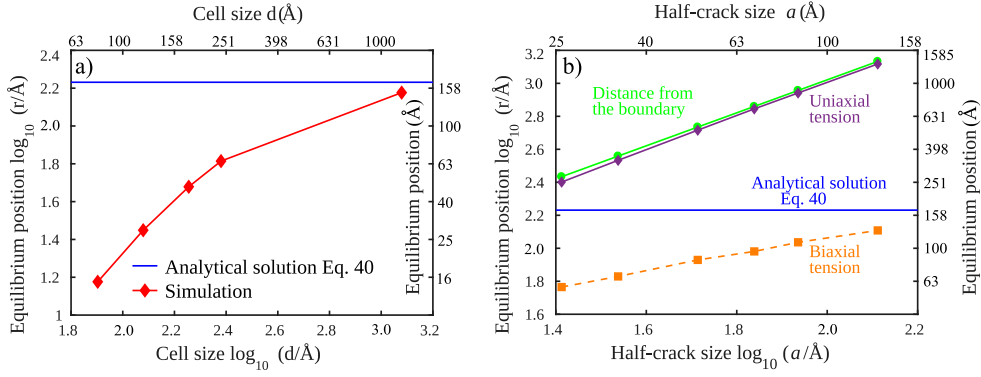


Figure 14. Equilibrium position r of the first partial dislocation after nucleation using (a) the K -test geometry and (b) the CCT test geometry under uniaxial and biaxial tension. The distance between the crack-tip and the outer CCT boundary along the slip plane (green circles) is shown for reference.

The equilibrium position of the first partial dislocation is then controlled only by the K -dominance zone, which itself depends on the crack size a . Therefore, the first partial dislocation is much closer to the crack tip (smaller r) ahead of short cracks, converging toward equation (40) for the largest crack size a . The huge difference in the partial position r between uniaxial and biaxial loading conditions shows clearly how the far-field (non-asymptotic) stresses lead to significant differences in behavior. For uniaxial tension, the partial dislocation has moved far outside the K -dominance domain, thus obviously violating the application of LEFM for any subsequent crack tip behavior, as discussed further below.

4.2.3. Dislocation/crack interaction: shielding effect. The stress field of the first partial dislocation at distance r on a slip plane inclined at angle θ creates additional crack-tip stress intensity factors k_j^d ($j = \text{I, II, III}$). Crack-tip shielding corresponds to $k_j^d < 0$ and anti-shielding to $k_j^d > 0$. In other words, the dislocation within the asymptotic crack-tip field generates an additional stress intensity factor at the crack tip that subtracts/adds to the far-field applied stress intensity. When the first partial is an edge dislocation, the shielding of a semi-infinite crack can be computed using LEFM [2, 59, 60] as

$$\begin{aligned} k_{\text{I}}^d &= -\frac{1}{2\sqrt{2\pi r}} \sum_{j=1}^3 \Lambda_{2j}^{-1} D_{2k}^j(\theta) b_k \\ k_{\text{II}}^d &= -\frac{1}{2\sqrt{2\pi r}} \sum_{j=1}^3 \Lambda_{1j}^{-1} D_{2k}^j(\theta) b_k \end{aligned} \quad (41)$$

with \mathbf{b} being the dislocation Burgers vector, $\mathbf{\Lambda}$ the Stroh tensor, and $\mathbf{D}^j(\theta)$ related to the angular distribution of stresses near the crack tip for the particular j mode of loading given in polar coordinates by

$$\sigma_{kl}(r, \theta) = \sum_{j=1}^3 \frac{1}{\sqrt{2\pi r}} K_j D_{kl}^j(\theta). \quad (42)$$

Note that an edge dislocation does not generate any k_{III}^d . Although the dislocation is an additional stress source that acts over the crack surfaces, the length scale requirement $r_{\text{FPZ}} \ll r_K \ll a$ is preserved. The FPZ for subsequent crack-tip events is again only the

atomistic region around the tip, aside from the residual stacking fault that is ignored due to elasticity purposes. Thus, the K -test geometry is again suitable model for obtaining insights into dislocation shielding effects. Since we deal with linear elasticity, the same model applies in the presence of multiple dislocations around the tip, as well. Therefore, the well-posed K -test enables investigation of the effects of far-field plasticity on overall fracture toughness [61].

The k_I^d and k_{II}^d , computed using equation (41), are exact solutions for semi-infinite cracks; therefore, we cannot use equation (41) for evaluating dislocation shielding of finite size cracks. Shielding of cracks having size of few nm is generally small, often negligible, as compared to semi-infinite cracks [62]. Thus, the nanoscale CCT test is not a quantitatively reliable approach for evaluating the shielding of cracks due to preexisting dislocations. Furthermore, under uniaxial loading where the first partial dislocation has moved far from the entire crack, any remaining shielding is sample size and geometry dependent.

4.2.4. Second partial dislocation emission. In fcc metals, such as Ni, further increase of the far-field applied stress intensity factor generates emission of a second partial dislocation. Within the (111)[$\bar{1}10$] crystal orientation and at $T = 0$ K, the only possible process is the emission of the twinning partial dislocation, which has the same character as the first partial but gliding on an immediately adjacent slip plane [63]. This crack-tip twinning can be predicted using the theory recently proposed by the authors [64], which is an extension of the Tadmor and Hai theory [63]. The remote critical stress intensity factor for crack-tip twinning K_{Ic}^{twin} in the presence of the first partial dislocation is

$$K_{Ic}^{twin} = f^{(1)}(C_{ijkl}) \left(\sqrt{(\gamma_{utf} - \gamma_{ssf})} o(\theta, \phi) / F_{12}(\theta) + k_I^d + \frac{F_{22}(\theta)}{F_{12}(\theta)} k_{II}^d \right), \quad (43)$$

where γ_{utf} is the unstable twinning fault energy, $f^{(1)}(C_{ijkl})$ is a material constant that correlates the far-field applied K_I and the stress intensity along the twinning slip plane, and $F_{22}(\theta)$ corrects for the resolved shear stress along the slip plane due to k_{II}^d . Twinning partial dislocation emission can be examined without the shielding by effectively moving the first partial dislocation to infinity [64]; in this special case equation (43) does not quite reduce to equation (32) since the stacking fault remains in the crack tip vicinity. Here, we examine the crack-tip twinning in the presence of the first partial dislocation.

We thus investigate crack-tip twinning using both the K -test and CCT test geometries. Figure 15 shows the K_{Ic}^{twin} for different cell sizes as measured in K -test atomistic simulations and as predicted by equation (43) in the presence of the first partial dislocation. As input in equation (41) we use the simulated position of the first partial dislocation r immediately before twinning occurs. Figure 15 shows K_{Ic}^{twin} increases as the simulation cell size decreases, which is due to (i) boundary effects as discussed above and, more importantly, (ii) the change in shielding since the equilibrium separation r is strongly affected by the sample boundary (see figure 14(a)). Note that fully converged results on crack-tip twinning require considerably larger simulation sizes. Decreasing the simulation cell size, we further observe a change of the twinning plane from behind the crack tip to ahead of the crack tip. More details on different twinning modes can be found in [64]. Overall, the K -test is shown to be a well-controlled, quantitatively and qualitatively precise approach to simulating atomic scale crack-tip events in the presence of far-field plasticity. However, when all dislocations are fully retained in the simulation, it is necessary that the simulation size be such that all dislocations are in their true (infinite material, infinite crack) positions so that their shielding/anti-shielding contributions are accurate. This size can be computationally infeasible, motivating

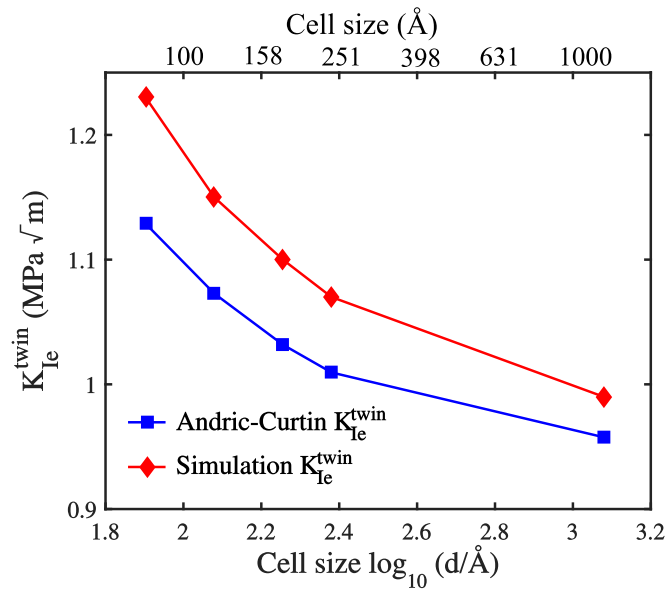


Figure 15. K -test results for the critical stress intensity factor for crack-tip twinning versus simulation cell size (red diamonds) along with the predictions of the LEFM based theory (blue squares).

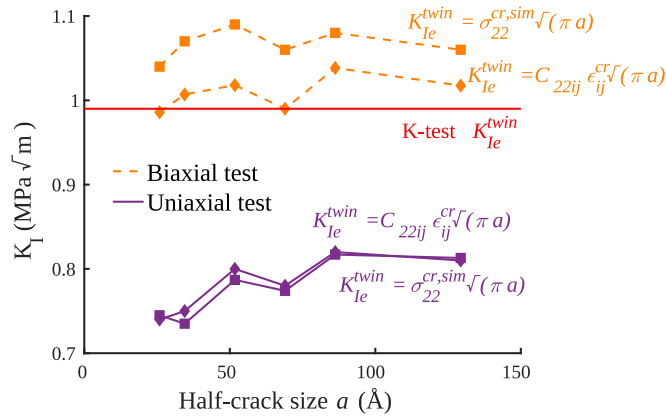


Figure 16. Computed critical stress intensity factor for crack-tip twinning $K_{Ie}^{twin} = \sigma_{22}^{cr} \sqrt{\pi a}$ versus crack size a in the CCT test simulations under uniaxial (purple solid lines) and biaxial (orange dashed lines) loading. Squares correspond to results computed using σ_{22}^{cr} directly from simulations, while diamonds correspond to results computed using $\sigma_{22}^{cr} = C_{22ij} \epsilon_{ij}^{cr}$. Solid red line: K -test results obtained using the largest simulation cell.

the development of multiscale methods to capture the dislocation plasticity away from the immediate crack tip (see section 5).

Figure 16 shows the CCT test results for the critical stress intensity factor for crack tip twinning computed using (i) uniaxial and (ii) biaxial tension tests along with the K -test results

obtained using the largest simulation cell (however not fully converged due to reasons discussed above). Note, once again, that we do not compare simulation results with the LEFM based theoretical predictions due to reasons that are discussed several times so far. We find K_{Ic}^{twin} depends on crack size, loading scenario, and calculation of σ^{cr} , as in every other case studied above. We notice K_{Ic}^{twin} to be much higher in biaxial than uniaxial tension; in other words twinning partial emission is much easier under uniaxial tension. The difference between two cases is due to (i) nonlinear response of the system and (ii) different shielding, since the first partial is much further from the crack tip in uniaxial tension (see figure 14 and section 4.2.2). Finally, good agreement between $K_{Ic}^{twin} = \sigma_{22}^{cr,sim} \sqrt{\pi a}$ and $K_{Ic}^{twin} = C_{22ij} \epsilon_{ij}^{cr} \sqrt{\pi a}$ in uniaxial tension is essentially a simulation artifact associated with $\sigma_{22}^{cr,sim}$ and the overall stress reduction due to emission of the first partial dislocation. As already discussed in section 4.1.2, the more precise method for estimating the $\sigma_{22}^{cr,sim}$ is to use the simulation cell without a crack and loaded at the critical applied strain ϵ^{cr} . All these results suggests that the nanoscale CCT test is not a suitable method for assessing fundamental material fracture properties, although the correct phenomena may be reproduced. What seems to be more important is that plasticity in front of a finite size crack is more easily triggered by phenomena outside of the FPZ, and therefore outside the domain of LEFM.

4.3. Fracture in an amorphous material

Fracture processes in amorphous materials is another active area where atomistic-scale simulations can provide insight into the nanoscale mechanisms of material failure. An amorphous material of high current interest is the Li–Si system, which is an emerging material for anodes in Li-ion batteries. Due to the large volume changes that the Li–Si material undergoes during charging and discharging of Li, the mechanics of Li–Si plays an important role in the cyclic fatigue (reduced storage and ultimate failure) of the battery system. Here, we use the Li–Si system as an entirely different example of the application of atomistic simulations to understanding nanoscale material failure. We do not repeat many of the important application-related details of the Li–Si fracture problem; these are well-covered in the original work [65]. Here, we focus solely on application of the atomistic fracture methodology.

Amorphous Li–Si is an elastic–plastic material. The plasticity is not dislocation-mediated, occurring instead by on-going operation of shear transformation zones. For the present purposes, the plasticity generates a plastic zone around the crack tip, and thus a FPZ. With a goal of computing the fracture toughness K_{Ic} , it is necessary to use the K -test method that has been advocated above. The high stresses that develop in CCT test simulations generally lead to plastic flow throughout the entire sample and thus the extraction of fracture toughness (the energy dissipated in the system associated with crack motion) is difficult. While the CCT test, and other fracture tests such as the strip geometry [66, 67], can reveal the local crack tip mechanisms of failure/fracture, they are not generally suitable for quantitative studies.

Sample preparation for amorphous materials requires special care, and is non-unique. Results here are obtained as follows. A Si simulation cell having dimensions of approximately $l_{x_1} = 120 \text{ \AA}$, $l_{x_2} = 108 \text{ \AA}$ and $l_{x_3} = 20 \text{ \AA}$ is created and then Li is added to create the desired Li_xSi compositions ($x = 0.5, 1.0, 1.5$). Relaxation of the system leads to a transformation to an amorphous structure. The system is then heated to the melting temperature of $T = 2500 \text{ K}$ and quenching to $T = 1 \text{ K}$ at a cooling rate of 500 K ns^{-1} . A large simulation cell for fracture studies is created by replicating the previously-prepared amorphous cell in a grid of $8 \times 7 \times 1 (x_1 \times x_2 \times x_3)$. The entire system is then heated to $T = 50 \text{ K}$ and quenched back to $T = 1 \text{ K}$. A semi-infinite crack with crack tip at $x_1 = 130 \text{ \AA}$ and $x_2 = 3.5l_{x_2}$ is

created using ‘screening’. These amorphous materials are elastic and plastically isotropic, with the elastic constants computed in separate MD studies in sufficiently large periodic cells of the material.

The crack is loaded to the desired applied K_I by imposing atomic displacements using equation (11). After each loading increment of $\Delta K_I = 0.01 \text{ MPa } \sqrt{\text{m}}$, atoms within 20 Å of the simulation outer boundary are held fixed, while all other atoms are allowed to relax using molecular dynamics at $T = 1 \text{ K}$. We perform sufficiently long relaxation until the total energy change between subsequent time steps is 10^{-6} eV/atom . Since amorphous materials are naturally out of equilibrium, and have a wide spectrum of relaxation times, the notion of absolute convergence is not useful. At low T , there is no significant long-time relaxation, however, and so the above strategy yields mechanical stable states at the desired applied load.

The Li–Si materials are elastic–plastic with yield strengths σ_y (in atomistic studies, meaning atomistic time scales of pico to nanoseconds) in the range of a few GPa. At an applied $K_I = 1 \text{ MPa } \sqrt{\text{m}}$, the plastic zone size can be estimated as $r_y = (K_I/\sigma_y)^2/3\pi$. This sets a scale for the FPZ that must be captured fully in the K -test simulations. Furthermore, under increasing applied K , the crack grows steadily during the simulation. That is, a so-called ‘resistance’ or R -curve develops, reflecting that the material is increasingly toughened as an unloaded plastic wake forms behind the crack tip. The existence of an R -curve thus requires that the system size be large enough to accommodate the total plastic zone up to the final fracture toughness K_{Ic} and that the boundary conditions properly reflect the actual crack tip position. The evolving crack tip position is found using coordination analysis to identify the largest position x_1 of newly-created crack surfaces. This procedure is accurate to $\pm 10 \text{ Å}$, which is sufficient for setting K boundary conditions in large simulation cells.

The above discussion is all aimed at maintaining the validity of SSY during the entire test. That SSY is satisfied must be explicitly examined in the simulations, as follows. Figure 17 shows atom-by-atom the von Mises equivalent stress $\tau_e = \sqrt{\frac{3}{2}(\boldsymbol{\sigma}^{\text{dev}} : \boldsymbol{\sigma}^{\text{dev}})}$, where $\boldsymbol{\sigma}^{\text{dev}} = \boldsymbol{\sigma} - \frac{1}{3}(\text{tr}\boldsymbol{\sigma})\mathbf{I}$ is the deviatoric stress tensor, normalized by the material yield stress σ_y (see table 2) at fracture initiation and at crack growth $\Delta a \approx 100 \text{ Å}$ for the three compositions studied here. Atom-by-atom stresses are computed using average virial stresses on all surrounding atoms within a radius $r \approx 6 \text{ Å}$. In most of the cases, the plastic zone r_{FPZ} is reasonably confined within the K -dominance zone r_K (simulation cell size). Note that the sporadic micro-plasticity away from the crack-tip is due to random nature of the Li_xSi glassy material, and does not correspond to large-scale plasticity. For the largest crack growth in the material with the lowest yield stress ($\text{Li } x = 1.5$), the plastic zone is starting to reach the boundaries of the simulation cell. Simulations are terminated at this point because the SSY assumption is no longer valid. Fortunately, however, while the SSY approximation may be violated in this case (see figure 17(f)), Rice formally proved that deviations from the dominant singular stress (applied through the boundary conditions), which exist here as fluctuations of the stress near the boundary, do not have a strong effect on the J -integral and fracture toughness [68]. Thus, although the simulation is pushing the limits of SSY, the associated measured fracture toughness remains reasonably accurate. Since the main focus of the work was precisely on the fracture toughness of Li_xSi system, the simulated results even for the low-yield stress material are deemed sufficiently accurate up to this stage of simulation.

It should be clearly noted that it is simply computationally infeasible to simulate much larger sizes that would better ensure LEFM and SSY, and it is impossible to use sizes that would be typical in continuum models. Therefore, the only solution is to push the limits of the SSY approximation, but with a good understanding how this might affect the quantitative results. Finally and most importantly, since the K -test simulation generally satisfies SSY, the

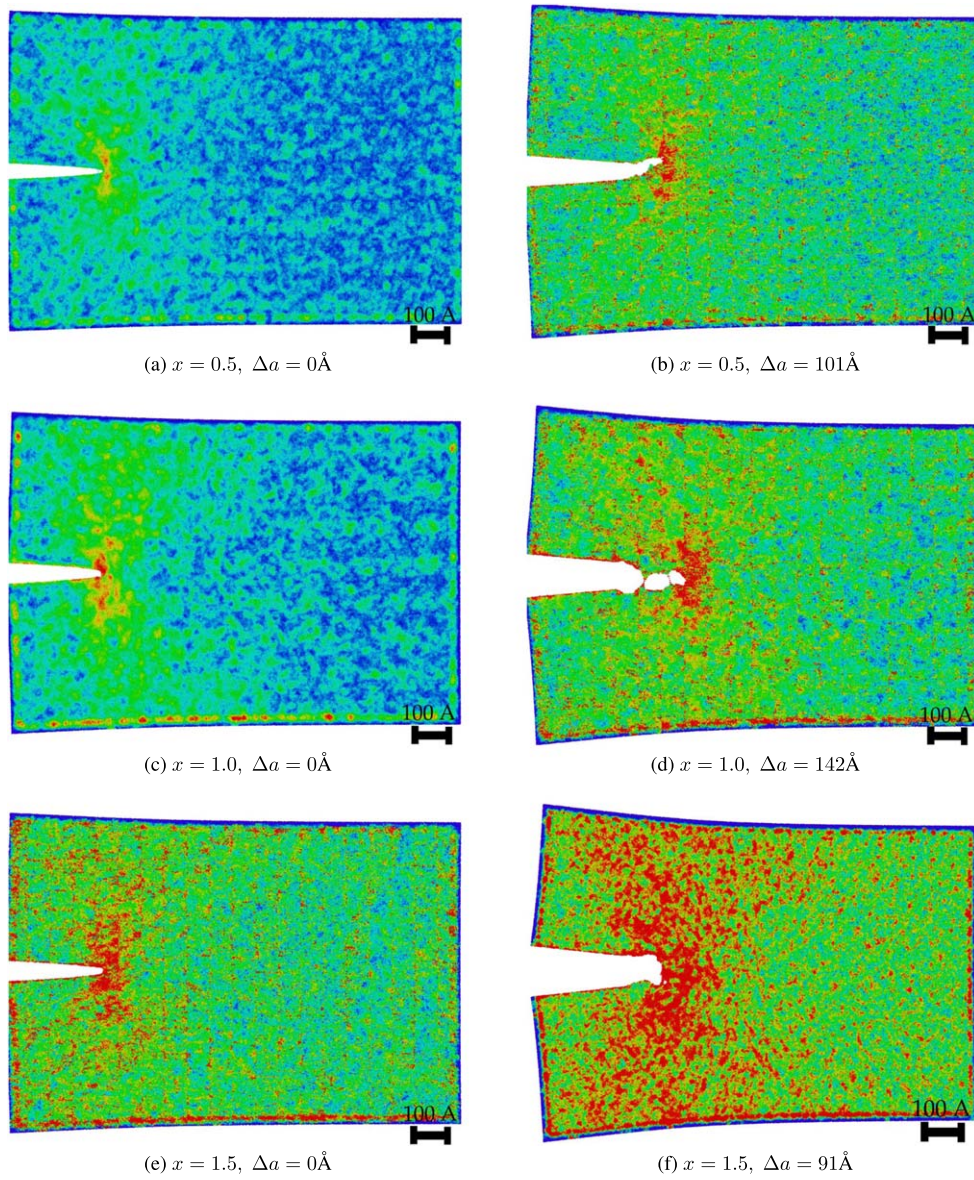
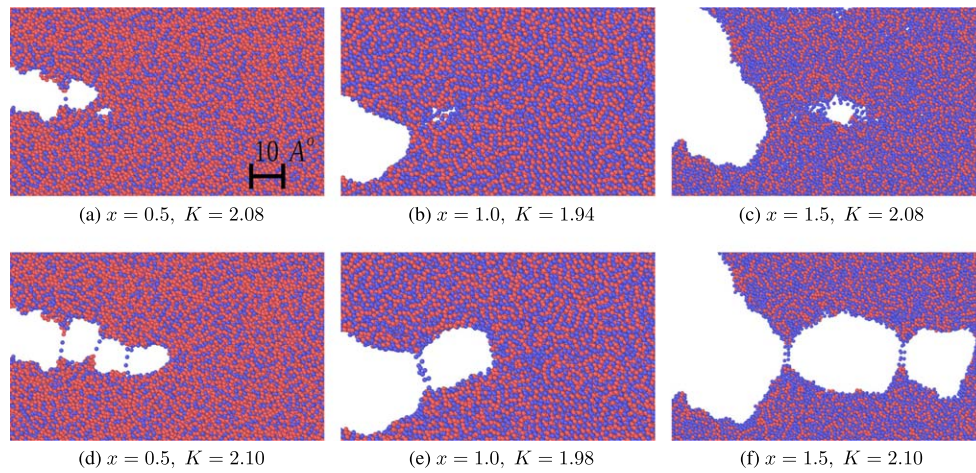


Figure 17. Snapshots of the fracture process in different samples, for $\Delta a = 0$ (onset of crack propagation) and $\Delta a \approx 100 \text{ \AA}$. The color coding is based on τ^e/σ_y (τ^e is the von Mises equivalent stress, and σ_y is the material yield strength) and red stands for $\tau^e/\sigma_y \geq 1$ and blue is $\tau^e/\sigma_y = 0$. Reprinted from [65], copyright 2017, with permission from Elsevier.

failure processes are attributable only to the singular stresses and the applied K_I , and not driven by unrealistic high far-field non-singular stresses. Thus, the fracture processes nearer to the tip are accurately captured. This overall discussion again highlights the need for a strong understanding of fracture mechanics theory when designing, executing, and interpreting atomistic simulations of fracture.

Table 2. Material properties of Li_xSi with different compositions. Reprinted from [65], copyright 2017, with permission from Elsevier.

x in Li_xSi	$E(\text{GPa})$	ν	$\sigma_y(\text{GPa})$
0.5	90.4	0.28	6.2
1.0	66.8	0.33	4.3
1.5	51.4	0.33	3.2

**Figure 18.** Subsequent snapshots of the creation and growth of a void during fracture process of samples with different composition (a), (d) $x = 0.5$, (b), (e) $x = 1.0$, (c), (f) $x = 1.5$. The scale is the same for all snapshots and is shown in the upper left picture. The spacing of voids in front of the crack is reproducible over multiple samples and different amounts of crack growth Δa . Reprinted from [65], copyright 2017, with permission from Elsevier.

The outcomes of the simulation are enlightening. The mechanism of failure is ductile void nucleation, growth, and coalescence, as shown in figure 18. As this process proceeds, the material is toughening, as shown by the R -curves for the different materials (see figure 19). Each amorphous sample having a finite crack front along x_3 is different in detail, leading to a range of R -curves for any given composition. Saturation of the R -curve corresponds to the establishment of a steady-state FPZ, with a plastic wake behind the growing crack tip. From the R -curves here, the materials at lower $x = 0.5, 1.0$ may be approaching saturation. However, the material at $x = 1.5$ may be continuing to toughen; to obtain fully converged results would require rather larger simulations.

The failure mechanism of void nucleation and coalescence is identical to the ductile fracture process observed in crystalline metals, but here at much smaller length scales. Using molecular dynamics simulations Robbins and collaborators [69, 70] found the similar failure mechanism in glassy polymers, as well. However, the failure mechanism in polymers cannot be assessed in direct atomistic fracture simulations since the FPZ size is on the order of tens of μm , far beyond molecular dynamics capabilities when actually modeling a crack tip. This limitation was addressed using representative volume regions that are subjected to different triaxial stress states which are in essence very similar to the stress state in front the crack tip. A similar analysis was also carried out for the Li-Si fracture [65].

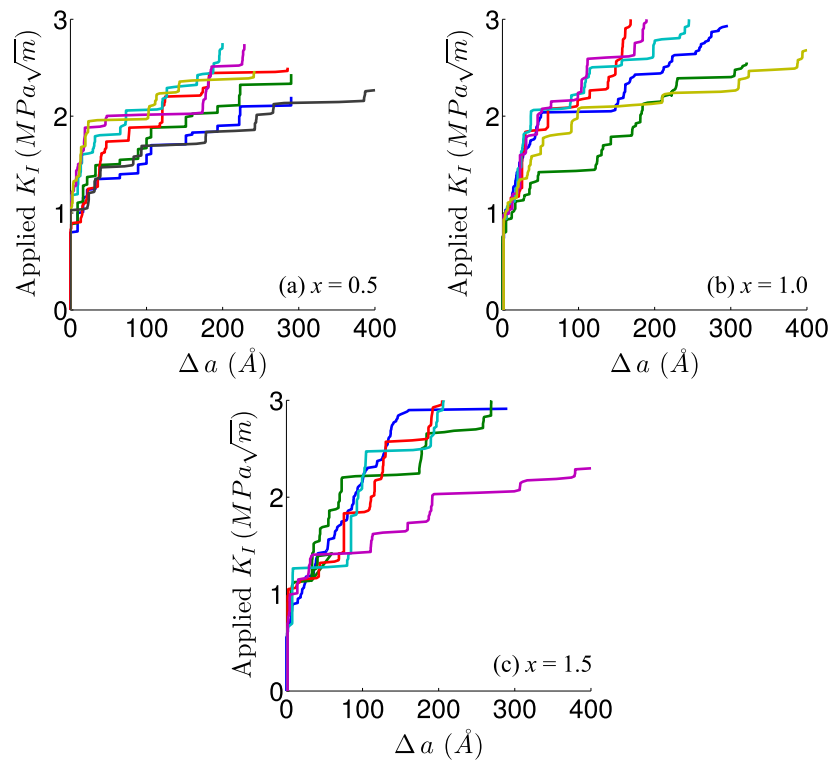


Figure 19. K_I versus crack length Δa , or R -curve, measured in MD simulations for three different Li compositions. For each composition, seven samples have been simulated to capture variations due to randomness in the amorphous structures. Reprinted from [65], copyright 2017, with permission from Elsevier.

Furthermore, having a robust set of simulations with quantitative toughness (for the interatomic potentials used here, which are only an approximation to the real material) enables analysis of the applicability of ductile fracture theory [71]. Ductile fracture models predict that the fracture energy is $\Gamma = \alpha \sigma_y D$ where $\alpha \sim 2$ is the scaling factor, and D is the spacing of the voids. The main insight gained from the atomistic simulations is that, although the amorphous elastic–plastic Li–Si fails by a ‘tough’ mechanism of ductile fracture, the toughness remains quite low because the voids nucleate at very small distances ($D \sim 1\text{--}2\text{ nm}$) ahead of the crack tip. Much greater detail on the fracture process and analysis can be found in [65]; our focus here is on the use of well-designed atomistic fracture modeling to reveal, qualitatively and quantitatively, the nanoscale fracture processes and fracture energies.

5. Discussion and summary

Atomistic modeling of fracture is now frequently being used to explore the behavior of crack-tip atoms in crystalline metals, alloys, ceramics, amorphous materials, and including the presence of different nanoscale defects. Here, we have critically analyzed several common simulation methods based on LEFM based methods. We have demonstrated that the atomic scale center-crack geometry often violates the basic concepts of SSY that is at the heart of the

application of LEFM. These tests violate the length scale hierarchy $r_{\text{FPZ}} \ll r_K \ll a$ and often introduce far-field (non-crack tip) nonlinear response and damage/plasticity due to the very high far-field applied stress needed to drive the desired crack-tip events. As a consequence, results obtained in the CCT test are not quantitative or general, and usually do not agree well with theoretical predictions. The problems that arise with the CCT test geometry are circumvented by the ‘*K*-test’ which uses a semi-infinite crack geometry controlled by an applied stress intensity K . By construction, the ‘*K*-test’ satisfies the concept of SSY, and provides results that are well-converged even at fairly small cell sizes, and results that generally agree well with the theoretical predictions. The advantages of the *K*-test have been demonstrated for both crystalline and amorphous materials.

We now discuss more advanced *K*-test simulation methods for investigating different processes associated with the atomically sharp crack tip. In the illustrative example shown in sections 4.2.1 and 4.2.4 we investigated the emission of the first and second (twinning) partial dislocation from a crack tip, respectively, but not further emission. The first emission is a vital process for crack blunting and toughening, but the overall fracture toughness is also governed (i) by the interaction between the crack tip and far-field plasticity (dislocations created by sources away from the crack tip itself) and (ii) continued (multiple) emission from the crack. The *K*-test atomistic model becomes computationally infeasible because the size of the real plastic zone would contain too many atoms. However, dislocations sufficiently far from the crack tip interact with the crack through elastic interactions only and, as we saw in the simple case of shielding of the crack by the first emitted partial dislocation, the elastic shielding/anti-shielding of cracks by dislocations can be computed analytically using elasticity theory, for plane-strain problems, and need not be directly simulated [21]. This then leads to the application of multiscale methods such as the coupled atomistic discrete dislocation (CADD) method [72, 73]. In CADD, the zone around the crack-tip is modeled with full resolution and so dislocation emission and fracture processes occurs naturally. Away from the crack tip, the material is described by the discrete dislocation (DD) plasticity model [74] in which continuum dislocations glide and interact with each other and with the crack via their elastic fields. The direct coupling of atomistics to continuum in CADD also enables the motion of dislocations into and out of the atomistic region in a seamless manner, such that the only approximation is, in principle, the elimination of the dislocation core structure for dislocations sufficiently far from the crack tip region. With such an approach, the *K*-test geometry is used in an identical manner, but effectively with two process zones, FPZ_{DD} and FPZ_{At} with FPZ_{DD} spanning the domain of the continuum dislocation plasticity and the much smaller FPZ_{At} contained within FPZ_{DD} ensuring proper atomistic response around the very high stress crack tip region.

Using interatomic potentials for simulating the atomistic region around the crack-tip is convenient if the potentials are sufficiently accurate. However, most of available interatomic potentials are not suitable for accurate description of real chemical effects on either brittle fracture or dislocation nucleation. These problems can again be circumvented by using a multiscale strategy in which the crack tip region is fully described by quantum mechanics while elasticity is used at further distances. The *K*-test method is applied with the *K* boundary conditions applied on the outer elasticity domain, enabling the use of a small quantum domain, and thus making the problem computationally tractable. Such a QM-CADD framework within the *K*-test geometry was developed to study the effects of hydrogen and oxygen on dislocation emission in aluminum [75, 76]. The *K*-test geometry has also been used in quantum mechanical/molecular mechanical (QM/MM) multiscale coupling method in silicon [77] and in aluminum [78]. In QM/MM, the region around the crack tip is again

simulated with quantum accuracy but coupled to a surrounding material domain simulated using classical interatomic potentials.

The present work provides the theoretical analysis followed by atomistic simulations of a semi-infinite cracks with periodic boundary conditions applied along the crack front under plane strain loading. Plane strain is not identical to 2D, however, and so the K -test can be applied to study some fully three-dimensional effects. Specifically, by using simulation cells having a sufficient length along the crack line direction it is possible to analyze problems such as (i) crack-tip dislocation emission on oblique slip planes, (ii) crack interactions with pre-existing 3D dislocation loops [79], (iii) crack-tip dislocation emission in alloys and multi-component solid solutions, and (iv) cleavage/dislocation emission from a crack-tip by kinks. Furthermore, the fracture simulations presented in this work were performed at $T = 0$ K. However, dislocation emission and other processes are thermally-activated with some K -dependent 3d nucleation (or transition) state. Nonetheless, the K -test geometry enables study of such 3d nucleation problems, e.g. [80–82].

Recent attention has also been given to the investigation of fully-embedded nanosize cracks (3d cracks), and the effects of crack front curvature on crack motion [83, 84]. It has been found that such embedded cracks are more prone to develop plastic zones ahead of the crack tip as compared to cracks with straight fronts under plane strain loading. However, special care must be taken in dealing with 3D cracks because they are finite sized and must be modeled in the 3D equivalent of CCT (a penny-crack geometry). 3D simulations thus suffer from the same challenges as 2D CCT tests. First, as in semi-infinite cracks, the fundamental length scale hierarchy $r_{\text{FPZ}} \ll r_K \ll a$ must be preserved, and the K -dominant zone remains comparable to that of 2D plain strain cracks. Embedded cracks of several nm diameter will quickly violate SSY after the first dislocation emission event. Secondly, as in the CCT case, the far-field applied stresses necessary to induce crack tip events are again extremely high, which introduces nonlinearities as noted also in [84]. Third, a high applied uniaxial stress generates high resolved shear stresses along different slip planes which act to drive dislocations far from the crack and generally to assist in creating plastic activity around the crack over sizes that may exceed the crack size itself. The pronounced plastic zone is thus not necessarily due to the nanocrack itself. Finally, nanoscale 3D cracks have high crack curvature that is not realistic for larger-scale cracks and which can introduce additional artificial effects. Therefore, the atomistic-scale simulation of fully-3D cracks must be approached with considerable care, and the present authors do not recommend such studies. The emergence of new fully-3D multiscale methods, specifically the generalization of CADD to 3D [85–87] may alleviate some of the above issues and expand our ability to study realistic 3D cracks both qualitatively and quantitatively.

As noted above, in many fracture problems the FPZ is immensely larger than the atomic scale so that direct MD simulations in the presence of a semi-infinite crack remain infeasible. In such cases, the variations in the stress field are then slow over atomistic scales, and local regions of material ahead of the crack can be envisioned as under some homogeneous loading state (uniaxial tension, triaxial stress, etc). In such cases, atomistic simulations can be used to study the FPZ response itself without the explicit crack tip. These studies are carried out on ‘representative’ volumes of material under a suitable stress state for the problem of interest. The work of Robbins *et al* [69, 70] on polymers, mentioned earlier, is one such example. Falk *et al* [88] and Khosrownejad *et al* [65] have carried out studies of the FPZ in amorphous metals and amorphous Li–Si, respectively. Tensile separation studies of crystalline materials and grain boundaries, with and without chemical segregation, have also been studied [50]. A full discussion and analysis of such methods is beyond the scope of the present paper. However, as with explicit-crack fracture tests, care must be taken to obtain quantitative results. For instance, the size of the ‘representative’ volume is often unknown *a priori*, and

the energy dissipation in a 3D simulation cell must be appropriately related to the expected dissipated energy in the actual fracture specimen. Size effects and boundary conditions also enter in subtle ways. Nonetheless, such studies are less problematic than explicit crack studies although less quantitative for relating to the true fracture problem.

To conclude, the examples presented in this paper demonstrate that accurate atomistic modeling of fracture should be based on the K -test geometry if possible. The use of finite-size embedded cracks, such as the CCT test, should be examined carefully in advance to ensure that none of the various issues/problems/artifacts identified here would strongly influence the results. In general, we do not recommend tests such as the CCT due to the difficulties in remaining within the limits of SSY and LEFM, but recognize that the K -test may not be useful for all problems of interest. Overall, use of the K -test demonstrates that a range of atomic scale fracture phenomena can be studied both qualitatively and quantitatively, providing valuable insight into the fundamental fracture of materials.

Acknowledgments

This work was supported by the European Research Council through the Advanced Grant ‘Predictive Computational Metallurgy’, ERC Grant agreement no. 339081 PreCoMet. The authors would also like to acknowledge the kind help of S M Khosrownejad in creating this review article.

Appendix. Effective elastic constants

Incorporating effects of nonlinearity for estimating the critical stress intensity factor for crack growth K_{Ic} requires proper cubic elastic constants as a function of the applied normal stress. We use molecular statics simulations for calculating the effective elastic constants in fcc Ni as follows. We define a simulation box, having periodic boundaries, oriented with $X_1 = [1\ 0\ 0]$, $X_2 = [0\ 1\ 0]$ and $X_3 = [0\ 0\ 1]$, and with dimensions in every direction of approximately 50 Å. We set desired stress perpendicular to the X_2 – X_3 plane by increasing lattice parameter in X_1 direction, while the lateral lattice parameter is held constant. At a given applied stress we compute C_{11} and C_{12} from the stress-strain response due to applied stress increment of $\Delta\sigma_{11} = 0.1$ MPa, while for estimating C_{44} we apply shear stress of $\tau_{12} = 0.1$ MPa. Figure 5 shows the elastic constants as a function of the applied stress. When the crystal orientation is aligned with the cubic axis we find that C_{11} can change up to 30% for the applied stress ~ 6 GPa. Furthermore, we use the same method for estimating elastic constant for tension along $[1\ 1\ 1]$ direction as a function of the applied stress. Figure 5 shows that within this crystal orientation elastic constant is less sensitive (up to $\sim 5\%$) and therefore we observe convergence in K_{Ic} for sufficiently big crack (see figure 13).

ORCID iDs

P Andric  <https://orcid.org/0000-0003-3768-201X>

References

- [1] Griffith A A and Eng M VI 1921 The phenomena of rupture and flow in solids *Phil. Trans. R. Soc. A* **221** 163–98
- [2] Rice J R and Thomson R 1974 Ductile versus brittle behaviour of crystals *Phil. Mag.* **29** 73–97

- [3] Rice J R 1992 Dislocation nucleation from a crack tip: an analysis based on the Peierls concept *J. Mech. Phys. Solids* **40** 239–71
- [4] Rice J R and Wang J S 1989 Embrittlement of interfaces by solute segregation *Mater. Sci. Eng. A* **107** 23–40
- [5] Chang R 1970 An atomistic study of fracture *Int. J. Fract. Mech.* **6** 111–25
- [6] Thomson R, Hsieh C and Rana V 1971 Lattice trapping of fracture cracks *J. Appl. Phys.* **42** 3154–60
- [7] Gumbsch P and Beltz G E 1995 On the continuum versus atomistic descriptions of dislocation nucleation and cleavage in nickel *Modelling Simul. Mater. Sci. Eng.* **3** 597
- [8] Gumbsch P 1995 An atomistic study of brittle fracture: toward explicit failure criteria from atomistic modeling *J. Mater. Res.* **10** 2897–907
- [9] Zhu T, Li J and Yip S 2004 Atomistic study of dislocation loop emission from a crack tip *Phys. Rev. Lett.* **93** 025503
- [10] Warner D H, Curtin W A and Qu S 2007 Rate dependence of crack-tip processes predicts twinning trends in fcc metals *Nat. Mater.* **6** 876
- [11] Wu Z and Curtin W A 2015 Brittle and ductile crack-tip behavior in magnesium *Acta Mater.* **88** 1–12
- [12] Miller R, Tadmor E B, Phillips R and Ortiz M 1998 Quasicontinuum simulation of fracture at the atomic scale *Modelling Simul. Mater. Sci. Eng.* **6** 607
- [13] Farkas D, Van Swygenhoven H and Derlet P M 2002 Intergranular fracture in nanocrystalline metals *Phys. Rev. B* **66** 060101
- [14] Möller J J and Bitzek E 2014 Fracture toughness and bond trapping of grain boundary cracks *Acta Mater.* **73** 1–11
- [15] Tehranchi A and Curtin W A 2017 Atomistic study of hydrogen embrittlement of grain boundaries in nickel: I. Fracture *J. Mech. Phys. Solids* **101** 150–65
- [16] Matsumoto R, Taketomi S, Matsumoto S and Miyazaki N 2009 Atomistic simulations of hydrogen embrittlement *Int. J. Hydrog. Energy* **34** 9576–84
- [17] Taketomi S, Matsumoto R and Miyazaki N 2010 Atomistic study of the effect of hydrogen on dislocation emission from a mode II crack tip in alpha iron *Int. J. Mech. Sci.* **52** 334–8
- [18] Song J and Curtin W A 2011 A nanoscale mechanism of hydrogen embrittlement in metals *Acta Mater.* **59** 1557–69
- [19] Song J and Curtin W A 2013 Atomic mechanism and prediction of hydrogen embrittlement in iron *Nat. Mater.* **12** 145
- [20] Wen M, Li Z and Barnoush A 2013 Atomistic study of hydrogen effect on dislocation nucleation at crack tip *Adv. Eng. Mater.* **15** 1146–51
- [21] Song J, Curtin W A, Bhandakkar T K and Gao H J 2010 Dislocation shielding and crack tip decohesion at the atomic scale *Acta Mater.* **58** 5933–40
- [22] Bitzek E and Gumbsch P 2008 Atomistic simulations of dislocation-crack interaction *J. Solid Mech. Mater. Eng.* **2** 1348–59
- [23] Gu X W, Jafary-Zadeh M, Chen D Z, Wu Z, Zhang Y W, Srolovitz D J and Greer J R 2014 Mechanisms of failure in nanoscale metallic glass *Nano Lett.* **14** 5858–64
- [24] Baker K L and Warner D H 2014 An atomistic investigation into the nature of near threshold fatigue crack growth in aluminum alloys *Eng. Fract. Mech.* **115** 111–21
- [25] Meng F, Chen C and Song J 2015 Dislocation shielding of a nanocrack in graphene: atomistic simulations and continuum modeling *J. Phys. Chem. Lett.* **6** 4038–42
- [26] Sumigawa T, Shimada T, Tanaka S, Unno H, Ozaki N, Ashida S and Kitamura T 2017 Griffith criterion for nanoscale stress singularity in brittle silicon *ACS Nano* **11** 6271–6
- [27] Gallo P, Yan Y, Sumigawa T and Kitamura T 2018 Fracture behavior of nanoscale notched silicon beams investigated by the theory of critical distances *Adv. Theory Simul.* **1** 1700006
- [28] Rice J R 1967 Stresses due to a sharp-notch in a work-hardening elastic-plastic material loaded by longitudinal shear *J. Appl. Mech.* **34** 287–98
- [29] Willis J R 1967 A comparison of the fracture criteria of Griffith and Barenblatt *J. Mech. Phys. Solids* **15** 151–62
- [30] Rice J R 1968 Mathematical analysis in the mechanics of fracture *Fracture: An Advanced Treatise (Mathematical Fundamentals vol 2)* ed H Liebowitz (New York: Academic) pp 191–311
- [31] Sun C T and Jin Z H 2012 *Fracture Mechanics* (Boston: Academic)
- [32] Anderson T L 2017 *Fracture Mechanics: Fundamentals and Applications* (Boca Raton, FL: CRC Press)

- [33] Gross D and Seelig T 2017 *Fracture Mechanics: With an Introduction to Micromechanics* (Berlin: Springer)
- [34] Muskhelishvili N I 2013 *Some Basic Problems of the Mathematical Theory of Elasticity* (Dordrecht: Springer Science and Business Media)
- [35] Westergaard H M 1939 Bearing pressures and cracks *J. Appl. Mech.* **6** A49–53
- [36] Irwin G R 1957 Analysis of stresses and strains near the end of a crack traversing a plate *J. Appl. Mech.* **24** 361–4
- [37] Ting T C 1996 *Anisotropic Elasticity: Theory and Applications* (Oxford: Oxford University Press)
- [38] Ingebrigtsen K A and Tonning A 1969 Elastic surface waves in crystals *Phys. Rev.* **184** 942
- [39] Irwin G R 1948 Fracture dynamics *Fracturing of Metals* (Cleveland, OH: American Society of Metals) pp 147–66
- [40] Orowan E 1952 Fundamentals of brittle behavior in metals *Fatigue Fract. Met.* **3** 139–67
- [41] Stroh A N 1958 Dislocations and cracks in anisotropic elasticity *Phil. Mag.* **3** 625–46
- [42] Sun Y and Beltz G E 1994 Dislocation nucleation from a crack tip: a formulation based on anisotropic elasticity *J. Mech. Phys. Solids* **42** 1905–32
- [43] Andric P and Curtin W A 2017 New theory for Mode I crack-tip dislocation emission *J. Mech. Phys. Solids* **106** 315–37
- [44] Pérez R and Gumbsch P 2000 Directional anisotropy in the cleavage fracture of silicon *Phys. Rev. Lett.* **84** 5347
- [45] Gumbsch P and Cannon R M 2000 Atomistic aspects of brittle fracture *MRS Bull.* **25** 15–20
- [46] Singh G, Kermode J R, De Vita A and Zimmerman R W 2014 Validity of linear elasticity in the crack-tip region of ideal brittle solids *Int. J. Fract.* **189** 103–10
- [47] Curtin W A 1990 On lattice trapping of cracks *J. Mater. Res.* **5** 1549–60
- [48] Bernstein N and Hess D W 2003 Lattice trapping barriers to brittle fracture *Phys. Rev. Lett.* **91** 025501
- [49] Mishin Y, Farkas D, Mehl M J and Papaconstantopoulos D A 1999 Interatomic potentials for monoatomic metals from experimental data and *ab initio* calculations *Phys. Rev. B* **59** 3393
- [50] Tehranchi A and Curtin W A 2017 Atomistic study of hydrogen embrittlement of grain boundaries in nickel: II. Decohesion *Modelling Simul. Mater. Sci. Eng.* **25** 075013
- [51] Rose J H, Smith J R and Ferrante J 1983 Universal features of bonding in metals *Phys. Rev. B* **28** 1835
- [52] Dugdale D S 1960 Yielding of steel sheets containing slits *J. Mech. Phys. Solids* **8** 100–4
- [53] Barenblatt G I 1962 The mathematical theory of equilibrium cracks in brittle fracture *Advances in Applied Mechanics* vol 7 (Amsterdam: Elsevier) pp 55–129
- [54] Stukowski A 2009 Visualization and analysis of atomistic simulation data with OVITO the open visualization tool *Modelling Simul. Mater. Sci. Eng.* **18** 015012
- [55] Plimpton S 1995 Fast parallel algorithms for short-range molecular dynamics *J. Comput. Phys.* **117** 1–9
- [56] Cui Z, Gao F, Cui Z and Qu J 2012 A second nearest-neighbor embedded atom method interatomic potential for Li–Si alloys *J. Power Sources* **207** 150–9
- [57] Bitzek E, Koskinen P, Gähler F, Moseler M and Gumbsch P 2006 Structural relaxation made simple *Phys. Rev. Lett.* **97** 170201
- [58] Song J, Soare M and Curtin W A 2010 Testing continuum concepts for hydrogen embrittlement in metals using atomistics *Modelling Simul. Mater. Sci. Eng.* **18** 045003
- [59] Lin I H and Thomson R 1986 Cleavage, dislocation emission, and shielding for cracks under general loading *Acta Metall.* **34** 187–206
- [60] Rice J R 1985 Conserved integrals and energetic forces *Fundamentals of Deformation and Fracture* (Cambridge: Cambridge University Press) pp 33–56
- [61] Ramasubramaniam A, Curtin W A and Farkas D 2002 Fracture in nanolamellar materials: continuum and atomistic models with application to titanium aluminides *Phil. Mag. A* **82** 2397–417
- [62] Zhang T Y and Li J C 1991 Image forces and shielding effects of an edge dislocation near a finite length crack *Acta Metall. Mater.* **39** 2739–44
- [63] Tadmor E B and Hai S 2003 A Peierls criterion for the onset of deformation twinning at a crack tip *J. Mech. Phys. Solids* **51** 765–93
- [64] Andric P and Curtin W A 2018 New theory for crack-tip twinning in fcc metals *J. Mech. Phys. Solids* **113** 144–61

- [65] Khosrownejad S M and Curtin W A 2017 Crack growth and fracture toughness of amorphous Li–Si anodes: Mechanisms and role of charging/discharging studied by atomistic simulations *J. Mech. Phys. Solids* **107** 542–59
- [66] Wang H and Chew H B 2016 Molecular dynamics simulations of plasticity and cracking in lithiated silicon electrodes *Extreme Mech. Lett.* **9** 503–13
- [67] Ding B, Li X, Zhang X, Wu H, Xu Z and Gao H 2015 Brittle versus ductile fracture mechanism transition in amorphous lithiated silicon: from intrinsic nanoscale cavitation to shear banding *Nano Energy* **18** 89–96
- [68] Rice J R 1974 Limitations to the small scale yielding approximation for crack tip plasticity *J. Mech. Phys. Solids* **22** 17–26
- [69] Baljon A R and Robbins M O 1996 Energy dissipation during rupture of adhesive bonds *Science* **271** 482–4
- [70] Rottler J and Robbins M O 2002 Jamming under tension in polymer crazes *Phys. Rev. Lett.* **89** 195501
- [71] Gurson A L 1977 Continuum theory of ductile rupture by void nucleation and growth: I. Yield criteria and flow rules for porous ductile media *J. Eng. Mater. Technol.* **99** 2–15
- [72] Curtin W A and Miller R E 2003 Atomistic/continuum coupling in computational materials science *Modelling Simul. Mater. Sci. Eng.* **11** R33
- [73] Shilkrot L E, Miller R E and Curtin W A 2004 Multiscale plasticity modeling: coupled atomistics and discrete dislocation mechanics *J. Mech. Phys. Solids* **52** 755–87
- [74] Van der Giessen E and Needleman A 1995 Discrete dislocation plasticity: a simple planar model *Modelling Simul. Mater. Sci. Eng.* **3** 689
- [75] Zamora R J *et al* 2012 *Ab initio* prediction of environmental embrittlement at a crack tip in aluminum *Phys. Rev. B* **86** 060101
- [76] Zamora R J, Baker K L and Warner D H 2015 Illuminating the chemo-mechanics of hydrogen enhanced fatigue crack growth in aluminum alloys *Acta Mater.* **100** 232–9
- [77] Kermode J R, Albaret T, Sherman D, Bernstein N, Gumbsch P, Payne M C, Csányi G and De Vita A 2008 Low-speed fracture instabilities in a brittle crystal *Nature* **455** 1224
- [78] Peng Q and Lu G 2011 A comparative study of fracture in Al: quantum mechanical versus empirical atomistic description *J. Mech. Phys. Solids* **59** 775–86
- [79] Bitzek E and Gumbsch P 2013 Mechanisms of dislocation multiplication at crack tips *Acta Mater.* **61** 1394–403
- [80] Zhu T, Li J and Yip S 2004 Atomistic study of dislocation loop emission from a crack tip *Phys. Rev. Lett.* **93** 025503
- [81] Yamakov V I, Warner D H, Zamora R J, Saether E, Curtin W A and Glaessgen E H 2014 Investigation of crack tip dislocation emission in aluminum using multiscale molecular dynamics simulation and continuum modeling *J. Mech. Phys. Solids* **65** 35–53
- [82] Warner D H and Curtin W A 2009 Origins and implications of temperature-dependent activation energy barriers for dislocation nucleation in face-centered cubic metals *Acta Mater.* **57** 4267–77
- [83] Ersland C H, Vatne I R and Thaulow C 2012 Atomistic modeling of penny-shaped and through-thickness cracks in bcc iron *Modelling Simul. Mater. Sci. Eng.* **20** 075004
- [84] Möller J J and Bitzek E 2015 On the influence of crack front curvature on the fracture behavior of nanoscale cracks *Eng. Fract. Mech.* **150** 197–208
- [85] Anciaux G, Junge T, Hodapp M, Cho J, Molinari J F and Curtin W A 2018 The coupled atomistic/discrete-dislocation method in 3D: I. Concept and algorithms *J. Mech. Phys. Solids* **118** 152–71
- [86] Hodapp M, Anciaux G, Curtin W A and Molinari J F 2018 Coupled atomistic/discrete dislocation method in 3D: II. Validation of the method *J. Mech. Phys. Solids* **119** 1–19
- [87] Cho J, Molinari J F, Curtin W A and Anciaux G 2018 The coupled atomistic/discrete-dislocation method in 3D: III. Dynamics of hybrid dislocations *J. Mech. Phys. Solids* **118** 1–4
- [88] Falk M L and Langer J S 1998 Dynamics of viscoplastic deformation in amorphous solids *Phys. Rev. E* **57** 7192